WILLIAM & MARY
CHARTERED 1693

Dissertations, Theses, and Masters Projects

Theses, Dissertations, & Master Projects

2023

Investigating The Environmental And Molecular Dependence Of Single-Molecule Blinking-Based Multiplexing

Grace DeSalvo
William & Mary - Arts & Sciences, gracedesalvo46@gmail.com

Follow this and additional works at: https://scholarworks.wm.edu/etd

Part of the Chemistry Commons

Investigating the Environmental and Molecular Dependence of Single-Molecule
Blinking-Based Multiplexing

Grace Anne DeSalvo

Glen Rock, New Jersey

Bachelor of Science, College of William & Mary, 2022

A Thesis presented to the Graduate Faculty of The College of William & Mary in
Candidacy for the Degree of
Master of Science

Department of Chemistry

College of William & Mary
August 2023

APPROVAL PAGE

This Thesis is submitted in partial fulfillment of
the requirements for the degree of

Master of Science
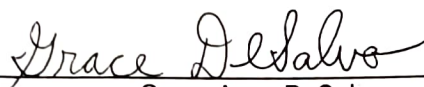
Grace DeSalvo

Grace Anne DeSalvo

Approved by the Committee, August 2023

Committee Chair
Kristin Wustholz, Professor, Chemistry
College of William & Mary

Nathan Kidwell, Associate Professor, Chemistry
College of William & Mary
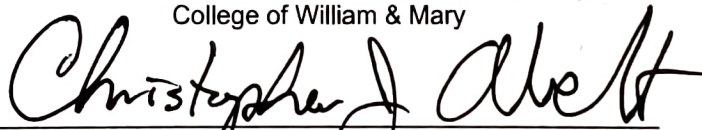
Christopher Abel, Chancellor Professor, Chemistry
College of William & Mary

ABSTRACT

Visualizing nanoscale biological systems allows us to uncover their detailed structure and functions, which have major implications in the biomedical field. Super-resolution microscopy is a powerful tool for fluorescence imaging because, by overcoming the diffraction limit of light, it accesses structural detail with unprecedented spatial resolution. Although multicolor super-resolution imaging has been successfully implemented in many experiments, its efficiency is limited by reliance on spectral measurement for emitter identification, which limits the combinations of compatible probes to be used together. Blinking-based multiplexing (BBM) is a novel approach that circumvents the need for spectrally-distinct emitters by instead exploiting the intrinsic differences in their blinking dynamics, or the stochastic fluctuations in emissive and nonemissive intensities of single-molecules under continuous photoexcitation. We find that BBM is most efficiently carried out using multinomial logistic regression (LR) to classify hundreds blinking dynamics obtained through single-molecule spectroscopy (SMS). Blinking dynamics are captured for three emitters—quantum dots (QD), rhodamine 6G (R6G), and pyrromethene 605 (PM605)— both on glass substrate and in complex poly(vinyl alcohol) (PVA) matrix for analysis with LR. Our results show that LR rapidly generates highly accurate predictive models for a variety of emitter systems under many experimental conditions.

TABLE OF CONTENTS

ACKNOWLEDGEMENTS

LIST OF TABLES

LIST OF FIGURES

Chapter 1: Introduction

1.1 Motivation: Imaging of Complex Biological Systems

The answers to many of the world's most urgent medical questions can be found by understanding the interactions between biomolecules. Uncovering key relationships between cellular structures such as proteins, membranes, DNA, RNA, and organelles facilitates research regarding disease states and healthy cellular function.[1,2] By gaining insight into the detailed structure of a cell, its organization, composition, and specialized activity can be uncovered, and more highly targeted drugs are developed. For instance, uncovering the catalytic function of an enzyme of interest may help researchers better understand how to design medicines with high binding affinity to outcompete the binding of toxins or other harmful molecules.[3] However, cellular components such as proteins, nuclei, membrane domains, and microtubules are typically on the nanometer to micrometer scale.[4] The small scale of these systems makes probing these components challenging.

Biological imaging through the detection of fluorescent molecules, also called fluorophores or emitters, is a powerful method for imaging on the nanoscale. Current imaging experiments are typically performed with multiple emitters so that more than one biological structure or component is labeled and studied. With the resulting multicolor images, researchers gain insight into the structure, function, and interactions within the sample. For instance, fluorescence images of nuclei have revealed heterogeneities in nuclear compartments as well as differences in chromatin organization based on cellular expression mechanism.[5,6] The insight gained from this

research has the potential to inform on DNA accessibility for potential repair or intervention of disease states.

Of course, multicolor biological imaging comes with experimental and analytical challenges, to be discussed later in greater depth. This thesis addresses these limitations by focusing on the development of novel methods for improving current multicolor techniques. First, for greater context on the importance of this work, the history of fluorescence imaging and the limitations of modern techniques are explored.

1.2 History of Single-Molecule Spectroscopy

Microscopy has been used for centuries to visualize biological structures. Robert Hooke first discovered the presence microorganisms in 1665 when he observed bread molds through his microscope.[7] However, early microscopes had low magnification and resolution, and therefore poor imaging capabilities. When measuring transmitted light in an optical microscope, high magnifications cause the resulting images to be distorted and appear as large, blurry circles called Airy disks. Even as developments in optics and lenses improved the performance of light microscopes over time, image quality continued to be hindered by the diffraction limit of light. First described by Ernst Abbe in 1873, the diffraction limit restricts imaging resolution.[8] The maximum resolution is dictated by $\lambda/(2 \times NA)$, where NA is the numerical aperture of the microscope and λ is the wavelength of light used for imaging.[9] Therefore, for visible wavelengths of light, structures <200 nm cannot be resolved.[4,9] The

shortcomings of conventional light microscopy limited the degree to which structural insight could be gained from micro- to nanoscale systems.

In 1845, an alternative imaging technique emerged when Sir Frederik William Herschel first reported on fluorescence. He observed that a transparent quinine solution emitted blue light when exposed to UV rays from the sun.[10] Researchers soon realized the potential of measuring emitted light for visualizing biological structures, as measuring signal that originates from the sample itself led to higher sensitivity and image contrast than transmitted or reflected light. The first fluorescence microscopes were developed in the early 1900s and were used to visualize biological structures using rudimentary fluorescent labeling techniques.[11] Image quality improved in the '40s and '50s when the advent of fluorescent antibody labeling allowed for greater specificity in tagging structures and Marvin Minsky built the first confocal microscope.[11–13] This instrument utilizes two pinhole apertures—one to focus the light source to a diffraction-limited spot on the plane of the sample and the other in front of the detector—to scan and detect emission from samples one point at a time. Although the full potential of confocal microscopy was not realized until after the invention of lasers, this development marked a major milestone in imaging.

Early optical measurements were taken at the bulk level, meaning that information was collected for an entire ensemble of molecules at once, and the resulting data described the average behavior of all the fluorophores. Due to the small size of individual molecules and the limited sensitivity of instruments at the time, studying single molecules was long considered an impossibility. Many believed that single

particles could only be evaluated in thought experiments and not in a physical laboratory. In fact, in the mid twentieth century, Schrödinger wrote "… it is fair to state that we are not *experimenting* with single particles, any more than we can raise Ichthyosauria in the zoo."[14] Eventually, in the 1980s, researchers started to gain direct access to nanoscale systems with advancements such as spectroscopy of single ions and electrons and the advent of scanning tunneling microscopy, but these experiments were only possible under vacuum.[15–17] The first optical detection of single molecules in condensed matter was reported in 1989, with the measurement of absorption spectra of pentacene in *p*-terphenyl host crystal at low temperatures.[18] These measurements, however, were collected using laser frequency-modulation spectroscopy (FMS), which suffered from poor signal-to-noise. The following year, Michel Orrit and Jacky Bernard made a significant breakthrough with the first fluorescence detection of single molecules in the same system.[19] Using a single wavelength, a laser was scanned across a pentacene sample, and single molecules were identified by measuring their emission with better signal to noise than FMS. With the inspiration and experimental foundation of these studies, as well as developments in lasers and highly sensitive cameras and detectors, the field of single-molecule spectroscopy (SMS) based on fluorescence detection emerged.[4]

Since its discovery in 1989, SMS has proved invaluable in several contexts, including uncovering new phenomena, nanoreporting, tracking, and localization. One important discovery that came out of SMS was the observation of blinking, a phenomenon on which much of thesis is based. Blinking refers to stochastic

fluctuations in the emissive intensity of a single molecule under continuous laser excitation. These changes occur as the molecule transitions between emissive and nonemissive states, also called "on" (bright) or "off" (dark) states, respectively. Historically, blinking has been modeled as a three-level system (**Figure 1**) where

intersystem crossing (ISC) to a triplet state interrupts fluorescence until the electron returns to the ground state.[20,21] In reality, dark states may arise from other processes, including proton transfer, electron transfer, quenching, and conformational changes, depending on the fluorophore and substrate properties.[20,22–24] An emitter undergoes
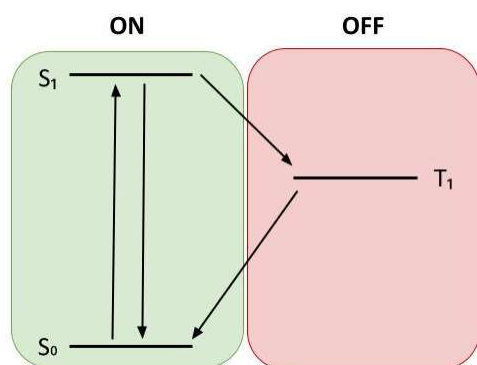
Figure 1. Energy level diagram demonstrating blinking involving the first triplet state (T_1). The singlet ground (S_0) and first excited (S_1) states translate to "on" events, and transitions to T_1 result in "off" events.

blinking until it becomes photobleached, meaning it has undergone an irreversible photochemical change that alters its excitation spectrum or renders it entirely nonfluorescent. Studying an emitter's photobleaching time and the durations of emissive and nonemissive events can reveal the photophysical mechanisms responsible for blinking.[22,23,25]

The discovery of blinking led to another application of SMS called nanoreporting. Single molecules are considered nanoreporters because their behavior relies on the conditions of the local environment; variations in solvent, substrate, molecular orientation, and excitation power are just a few of many factors that may influence a fluorophore's behavior.[4,9] Nanoreporting gives SMS the power to uncover

heterogeneities within samples that are otherwise hidden by ensemble averaging. Ensemble averaging obscures the true shape of a distribution because it only offers insight regarding the mean properties of the emitter. In other words, the true distribution of a particular emitter property may be skewed to either side, approximately normal, uniform, bimodal, etc., but the average value gives no indication of the full distribution underlying the average. By probing molecules individually, SMS allows researchers to build up distributions one molecule at a time, giving deeper insight into molecular behavior and the complex local environment.

SMS nanoreporting can be used to reveal both static and dynamic properties of emitters or tagged systems. For instance, protein folding and unfolding can be analyzed using Förster resonance energy transfer (FRET) to detect conformational changes on the order of angstroms.[26] In one single-molecule confocal microscopy study, researchers determined the distance between flavin, a fluorescent protein, and a nearby quenching tyrosine residue through fluorescence decay measurements taken under various experimental conditions.[27] Flavin adenine dinucleotide (FAD), one variety of the protein, plays a role in DNA synthesis through its reduction by protonated nicotinamide adenine dinucleotide (NADH), an important molecule in energy production. FAD is fluorescent in its oxidized form but not when it is reduced to FADH. Therefore, the observation of fluorescence indicates a reversible redox reaction taking place. Taking advantage of this flip between emissive and nonemissive forms, the enzymatic kinetics of FAD reduction have been tracked to determine the impacts of

conformation on catalytic rate and efficiency.[28] This example describes just one of many biological processes that has been enlightened using SMS nanoreporting.

SMS is also commonly used for tracking and localization. By detecting the fluorescence given off by an individual emitter, its position in space and time can be estimated. This application is useful for monitoring the movement of emitters or tagged structures over time. Tracking has elucidated many nanoscale processes, including shuttling proteins and viruses across cell membranes, DNA repair, and drug delivery.[29–33] In addition to informing on dynamic processes, SMS can be used to localize static emitters on fluorescently tagged structures. Conventional fluorescence microscopy may be used for such visualization, but image quality is limited by the diffraction limit of light. Therefore, emitters, which are each approximately 1 nm in size, appear as large, blurry spots known as the point-spread function (PSF) of the microscope.[9] To overcome this challenge, super-resolution imaging (SRI) was developed to create images of nanoscale systems with unprecedented spatial resolution.

1.3 Super-Resolution Imaging

Super-resolution microscopy overcomes the diffraction limit through precise localization of single fluorescent probes.[34,35] The concept of SRI is that a nanoscale structure of interest is densely labeled with fluorescent probes, and these single-molecules are individually localized through their emission after illuminating the sample with laser excitation. The selected emitters may be organic dyes, fluorescent proteins, semiconductor nanoparticles, or fluorescent oligonucleotides depending on

the method employed and the conditions of the experiment.[4,36–39] If all the emitters on a tagged structure were to fluoresce simultaneously, as in previous imaging techniques, their PSFs would overlap, and no single molecules could be resolved.[4] To avoid this issue, SRI utilizes an active control mechanism, which can be either chemical or optical in nature, to limit the number of emitters that are detected at once and temporarily allow for spatial resolution of adjacent molecules. For two fluorophores in close proximity, if one fluoresces while the other is dark, only one PSF will be detected, and the molecules will temporarily be spatially resolved. Processes such as blinking, photoactivation, photoswitching, and photobleaching are commonly used to limit the number of molecules that emit at any given moment.[4,40–44] Once PSFs of single emitter are detected, they are fit to an appropriate function, typically a 2D Gaussian, and their locations can be estimated at the center with low uncertainty.[4] Consequently, the width of the PSFs shrinks considerably, and emitters can be localized with precision on the order of tens (instead of hundreds) of nanometers. After localizing each of the detected molecules, a pointillistic image of the structure of interest can be constructed based on the analytically-determined positions.[45]

There are many approaches to super-resolution microscopy that have been utilized for imaging experiments. The general principles described above for the creation of a reconstructed image stay relatively consistent for each, but the active control mechanisms vary between techniques. One of the early forms of super-resolution imaging, which was developed in 1994, is stimulated emission depletion (STED) confocal laser scanning microscopy.[13] In this method, an excitation laser is

used to spur fluorescence in a focused area on the structure of interest. A second, doughnut-shaped laser creates a tight circle around the excitation source and forces the molecules it hits to the ground state by inducing stimulated emission.[46,47] The redder wavelength, or lower energy, of the depletion laser causes the fluorophores to undergo stimulated emission rather than excitation. While in the ground state, the molecules will not fluoresce, so a single molecule at the center of the ring can be localized without any overlapping signal. Despite success in utilizing STED due to the high degree of active control over fluorescence, the technique comes with a few disadvantages.[48–50] The high power of the depletion laser may cause molecular photobleaching, meaning the affected emitters can no longer fluoresce and will no longer be detected, decreasing image quality. Additionally, live biological systems are sensitive to intense light, so the structures of interest may be damaged.[36]

To improve upon the limitations of STED, another class of imaging techniques called single-molecule localization microscopy (SMLM) was developed.[51] SMLM allows for spatial resolution of emitters through active control mechanisms such as photoactivation, photoswitching, and blinking (**Figure 2**). Whereas STED localizes
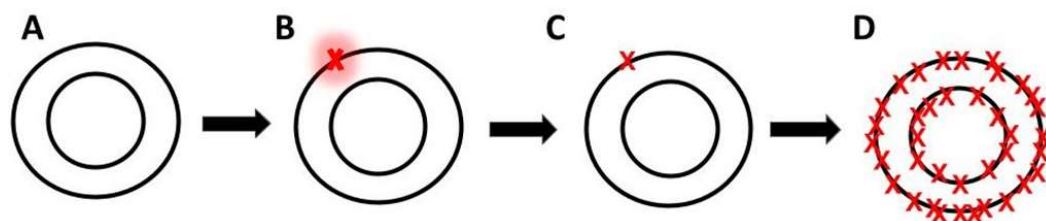
Figure 2. Principle of SMLM. (A) A nanoscale structure of interest is labeled with fluorophores. (B) Emission is detected from individual molecules through an active control mechanism (e.g., photoactivation, photoswitching, or blinking), which (C) allows for precise localization. (D) After many data points are collected, a reconstructed image reveals structural intricacies.

fluorophores one at a time through confocal scanning of a well-defined region, SMLM utilizes wide-field acquisition to collect data on small subsets of emitters at once.[13] Eliminating the need for a depletion laser source for single point localization (as seen in STED) reduces the amount of active control available over blinking, but, as a tradeoff, simplifies experimental design and reduces sample destruction.

Multiple methods fall underneath the category of SMLM. Photoactivated localization microscopy (PALM) and stochastic optical reconstruction microscopy (STORM) are two examples of SMLM techniques that follow similar procedures. Both techniques rely on photoactivation, photodeactivation (i.e., photobleaching), and photoconversion to reduce the density of molecules fluorescing at once.[13] A difference between the two methods is the type of emitter employed: fluorescent proteins for PALM and organic fluorophores for STORM.[36,52] Additionally, with STORM, data acquisition is quickened by simultaneously photoactivating and imaging the fluorophores, whereas these steps are performed sequentially in PALM.[53] Points accumulation for imaging in nanoscale topography (PAINT), a third variety of SMLM, induces blinking from the binding and unbinding events of fluorophores on the structure being imaged.[4,37] When bound, the molecules fluoresce, and they enter a dark state upon unbinding. Often, the emitters of choice are fluorescent oligonucleotides, or short single-stranded DNA coupled to fluorophores. In this case, there are docking strands attached to the structure of interest, and the fluorescently-labeled imaging strand transiently binds to them.[37] The fact that the emissive events of DNA-PAINT

rely on binding rather than blinking and molecular photophysics sets this SMLM technique apart from the others.

1.4 Challenges with Multicolor SMLM

Although much can be learned from single-fluorophore studies, the advancement of the biological imaging field relies on the implementation of multicolor imaging. By imaging multiple cellular components at once, researchers gain greater insight into their structure, functions, and interactions. However, this endeavor is much more challenging than single-probe imaging, as more than one distinct emitter must be used. Although several groups have demonstrated successful implementation of multicolor imaging techniques, multiple obstacles currently stand in the way of streamlining the effectiveness and efficiency of these experiments.[4,49]

One complicating factor is that despite the wide array of available fluorescent probes, finding suitable combinations of these emitters is challenging. Ideally, the fluorophores should be compatible under the same experimental conditions, including solvent and excitation power. Additionally, the fluorophores must be distinguishable through spectral measurement, meaning their emission spectra must be distinct (i.e., separated by >100 nm) in order to limit spectral crosstalk.[54] To resolve this issue, researchers typically image each emitter sequentially, which requires multiple laser excitation sources and adds significantly to data collection time and cost.[55–57] Some studies have attempted to circumvent these numerous issues by using methods such as combinatorial labeling and spectral barcoding as well as signal demixing from a single

spectral channel, but these advances have not helped to expand the limited set of compatible high-performance emitters.[2,58,59]

Another potential alternative to the limited palette of fluorophores for multicolor imaging is the use of DNA-PAINT. With his technique, fluorescent events occur due to binding events rather than intrinsic dye photoswitching properties, which makes it compatible to be used with a wider selection of fluorophores. However, this technique has several complications, such notoriously long data acquisition times and nonspecific binding.[37,57,60] Consequently, there is a need for alternative multicolor imaging methods that involve faster, simpler experimental and analytical demands as well as an expansive library of available fluorescent probes. This thesis describes the study of single-molecule blinking dynamics for the development of blinking-based multiplexing (BBM), a novel imaging tool that eliminates the issues of current multicolor imaging techniques.

1.5 Methods

Although BBM is intended for use in SMLM, all experiments described in this work are carried out using the available instrumentation: a confocal fluorescence microscope. Despite being a diffraction-limited technique, thus limiting its resolution, confocal microscopy is capable of probing single-emitter blinking dynamics so long as they are spatially isolated.

1.5.1 Single-Molecule Confocal Microscopy

In a single-molecule confocal experiment, individual emitters are detected by their fluorescence under continuous laser excitation on a confocal microscope. To ensure that only one emitter is studied at a time, samples are diluted to nanomolar concentrations. The resulting solutions are spin coated onto glass slides, which are secured onto a custom-designed flow cell and placed onto a piezoelectric stage above the objective. A schematic of a confocal microscope setup is depicted in **Figure 3**. The collimated laser beam is directed into the microscope, where it passes sequentially through an
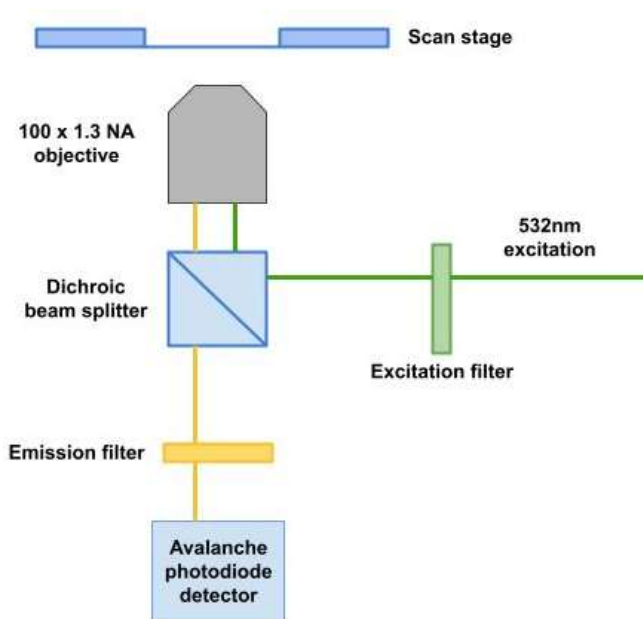
Figure 3. Schematic of a confocal microscope setup for a single-molecule experiment.

excitation filter, a dichroic beam splitter, and an objective to reach the sample. The objective focuses the collimated light to a diffraction-limited spot at the sample. The numerical aperture (NA) of the objective dictates the instrument's ability to gather light and therefore impacts the maximum achievable resolution. For instance, a NA of 1.3 and an excitation wavelength of 532 nm gives a theoretical diffraction limit of ~200 nm. When the focused laser beam reaches the sample, emitters are excited and emit red-shifted fluorescence. The emitted photons pass back down through the objective

and the beam splitter before reaching an emission filter, which blocks out all wavelengths as energetic or more energetic than the excitation source. Lastly, the emission is directed to an avalanche photodiode detector (APD).

Using a piezoelectric stage to induce fine, precise movement in the sample, a 10-100 μm² area of the sample is raster scanned. The resulting image visualizes the emission at each point in the scan in units of photons per bin time (typically 10-100 ms). A representative image of quantum dots (QD) immobilized on a glass substrate is shown in **Figure 4**, where each colored circle, bright and dim alike, is a diffraction-limited spot of a single emitter.
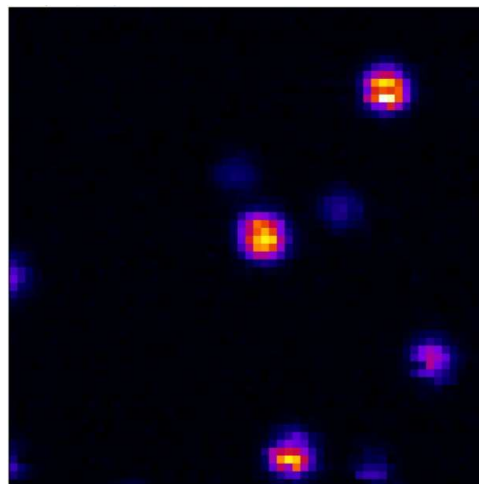
Figure 4. A representative 6x6μm false-colored image of 0.8 nM QD on glass.

1.5.2   *Single-Molecule Blinking Dynamics*

Measuring blinking dynamics at each diffraction-limited spot confirms the presence of single emitters and probes their photophysical behavior. Blinking dynamics are obtained through the collection of blinking traces (**Figure 5**), which are graphs measuring emission dynamics from a single molecule over time in units of counts per bin time. High emission counts indicate that the emitter is in a bright state, whereas low or baseline counts indicate a dark state or the occurrence of photobleaching. The traces are analyzed using change point detection (CPD) analysis, as simple thresholding does
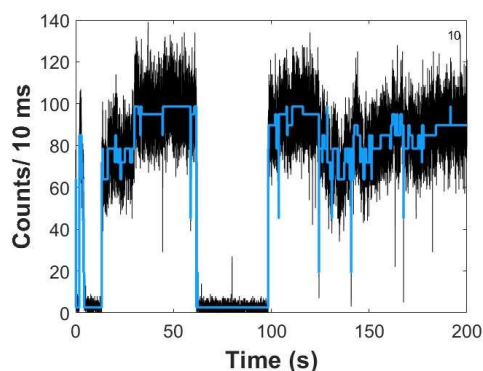
Figure 5. A representative blinking trace of a single CdSe/ZnS quantum dot on a glass substrate. The black line represents the raw data of photon emission per dwell time, and the blue overlay shows the on/off segments and intervals detected by CPD. The number of distinct intensity levels is displayed in the top right corner.

not hold the same accuracy and detail in determining emissive events.[24,61] CPD uses generalized likelihood tests to determine statistically significant fluctuations in intensity levels, which gives the capability not only to determine whether a molecule is "on" or "off" but also to detect smaller segments within the larger intervals.[62] An interval refers to the entire length of time that a molecule is either on or off, whereas a segment refers to the length of time a molecule remains at a single intensity within said interval. Consequently, segments are less than or equal to intervals in length. The blue overlay in **Figure 5** visually depicts the on/off segments/intervals determined by CPD. From these determinations, CPD outputs fourteen statistics that give insight into the photophysical properties of the emitter, including average on and off segment and interval times, average intensity (or photon counts), and switching frequency (the number of segment or interval events per second).

1.6 Thesis Outline

This thesis describes the use of blinking dynamics of three spectrally-overlapped emitters— quantum dots (QD), rhodamine 6G (R6G), and pyrromethene 605 (PM605)—for the development of a new multicolor imaging tool: blinking-based

multiplexing (BBM). Chapter 2 delves into the creation of BBM with a QD/R6G system and refinement with machine learning techniques to ensure rapid, accurate, and generalizable methodology. Chapter 3 investigates the application of BBM to emitters in a complex polymer environment to establish its viability for use in biological applications. Furthermore, the chapter uses blinking dynamics to identify the photophysical mechanism behind PM605 blinking and introduces this fluorophore as a third probe for use in BBM.

References

(1)   Cohen, S.; Valm, A. M.; Lippincott-Schwartz, J. Interacting Organelles. *Curr. Opin. Cell Biol.* **2018**, *53*, 84–91. https://doi.org/10.1016/j.ceb.2018.06.003.

(2)   Valm, A. M.; Cohen, S.; Legant, W. R.; Melunis, J.; Hershberg, U.; Wait, E.; Cohen, A. R.; Davidson, M. W.; Betzig, E.; Lippincott-Schwartz, J. Applying Systems-Level Spectral Imaging and Analysis to Reveal the Organelle Interactome. *Nature* **2017**, *546* (7656), 162–167. https://doi.org/10.1038/nature22369.

(3)   Dubach, J. M.; Vinegoni, C.; Mazitschek, R.; Fumene Feruglio, P.; Cameron, L. A.; Weissleder, R. In Vivo Imaging of Specific Drug–Target Binding at Subcellular Resolution. *Nat. Commun.* **2014**, *5* (1), 3946. https://doi.org/10.1038/ncomms4946.

(4)   Möckl, L.; Moerner, W. E. Super-Resolution Microscopy with Single Molecules in Biology and Beyond–Essentials, Current Trends, and Future Challenges. *J. Am. Chem. Soc.* **2020**, *142* (42), 17828–17844. https://doi.org/10.1021/jacs.0c08178.

(5)   Szczurek, A.; Xing, J.; Birk, U. J.; Cremer, C. Single Molecule Localization Microscopy of Mammalian Cell Nuclei on the Nanoscale. *Front. Genet.* **2016**, *7*.

(6)   Bohn, M.; Diesinger, P.; Kaufmann, R.; Weiland, Y.; Müller, P.; Gunkel, M.; von Ketteler, A.; Lemmer, P.; Hausmann, M.; Heermann, D. W.; Cremer, C. Localization Microscopy Reveals Expression-Dependent Parameters of Chromatin Nanostructure. *Biophys. J.* **2010**, *99* (5), 1358–1367. https://doi.org/10.1016/j.bpj.2010.05.043.

(7)   *The discovery of microorganisms by Robert Hooke and Antoni van Leeuwenhoek, Fellows of The Royal Society*. https://doi.org/10.1098/rsnr.2004.0055.

(8)   Abbe, E. Beiträge zur Theorie des Mikroskops und der mikroskopischen Wahrnehmung. *Arch. Für Mikrosk. Anat.* **1873**, *9* (1), 413–468. https://doi.org/10.1007/BF02956173.

(9)   Moerner, W. E. (William E.). Nobel Lecture: Single-Molecule Spectroscopy, Imaging, and Photocontrol: Foundations for Super-Resolution Microscopy. *Rev. Mod. Phys.* **2015**, *87* (4), 1183–1212. https://doi.org/10.1103/RevModPhys.87.1183.

(10)   Herschel, J. F. W. IV. Ἀμόρφωτα, No. I.— on a Case of Superficial Colour Presented by a Homogeneous Liquid Internally Colourless. *Philos. Trans. R. Soc. Lond.* **1997**, *135*, 143–145. https://doi.org/10.1098/rstl.1845.0004.

(11)   Renz, M. Fluorescence Microscopy—A Historical and Technical Perspective. *Cytometry A* **2013**, *83* (9), 767–779. https://doi.org/10.1002/cyto.a.22295.

(12)   Coons, A. H.; Creech, H. J.; Jones, R. N.; Berliner, E. The Demonstration of Pneumococcal Antigen in Tissues by the Use of Fluorescent Antibody1. *J. Immunol.* **1942**, *45* (3), 159–170. https://doi.org/10.4049/jimmunol.45.3.159.

(13) Birk, U. J. *Super-Resolution Microscopy: A Practical Guide*; John Wiley & Sons, Incorporated: Newark, GERMANY, 2017.

(14) Schrödinger, E. Are There Quantum Jumps? Part II. *Br. J. Philos. Sci.* **1952**, *3* (11), 233–242.

(15) Itano, W. M.; Bergquist, J. C.; Wineland, D. J. Laser Spectroscopy of Trapped Atomic Ions. *Science* **1987**, *237* (4815), 612–617. https://doi.org/10.1126/science.237.4815.612.

(16) Binnig, G.; Rohrer, H. Scanning Tunneling Microscopy—from Birth to Adolescence. *Rev. Mod. Phys.* **1987**, *59* (3), 615–625. https://doi.org/10.1103/RevModPhys.59.615.

(17) Diedrich, F.; Krause, J.; Rempe, G.; Scully, M. O.; Walther, H. Laser Experiments with Single Atoms as a Test of Basic Physics. *IEEE J. Quantum Electron.* **1988**, *24* (7), 1314–1319. https://doi.org/10.1109/3.968.

(18) Moerner, W. E.; Kador, L. Optical Detection and Spectroscopy of Single Molecules in a Solid. *Phys. Rev. Lett.* **1989**, *62* (21), 2535–2538. https://doi.org/10.1103/PhysRevLett.62.2535.

(19) Orrit, M.; Bernard, J. Single Pentacene Molecules Detected by Fluorescence Excitation in a *p* -Terphenyl Crystal. *Phys. Rev. Lett.* **1990**, *65* (21), 2716–2719. https://doi.org/10.1103/PhysRevLett.65.2716.

(20) Zondervan, R.; Kulzer, F.; Orlinskii, S. B.; Orrit, M. Photoblinking of Rhodamine 6G in Poly(Vinyl Alcohol): Radical Dark State Formed through the Triplet. *J. Phys. Chem. A* **2003**, *107* (35), 6770–6776. https://doi.org/10.1021/jp034723r.

(21) Yip, W.-T.; Hu, D.; Yu, J.; Vanden Bout, D. A.; Barbara, P. F. Classifying the Photophysical Dynamics of Single- and Multiple-Chromophoric Molecules by Single Molecule Spectroscopy. *J. Phys. Chem. A* **1998**, *102* (39), 7564–7575. https://doi.org/10.1021/jp981808x.

(22) Tan, J. A.; Garakyaraghi, S.; Tagami, K. A.; Frano, K. A.; Crockett, H. M.; Ogata, A. F.; Patterson, J. D.; Wustholz, K. L. Contributions from Excited-State Proton and Electron Transfer to the Blinking and Photobleaching Dynamics of Alizarin and Purpurin. *J. Phys. Chem. C* **2017**, *121* (1), 97–106. https://doi.org/10.1021/acs.jpcc.6b09818.

(23) Tan, J. A.; Rose, J. T.; Cassidy, J. P.; Rohatgi, S. K.; Wustholz, K. L. Dispersive Electron-Transfer Kinetics of Rhodamines on TiO2: Impact of Structure and Driving Force on Single-Molecule Photophysics. *J. Phys. Chem. C* **2016**, *120* (37), 20710–20720. https://doi.org/10.1021/acs.jpcc.6b01960.

(24) Lynch, P. G.; Richards, H.; Wustholz, K. L. Unraveling the Excited-State Dynamics of Eosin Y Photosensitizers Using Single-Molecule Spectroscopy. *J. Phys. Chem. A* **2019**, *123* (13), 2592–2600. https://doi.org/10.1021/acs.jpca.9b00409.

(25) Kopera, K. M.; Tuckman, H. G.; Hoy, G. R.; Wustholz, K. L. Origin of Kinetic Dispersion in Eosin-Sensitized TiO2: Insights from Single-Molecule Spectroscopy. *J. Phys. Chem. C* **2021**, *125* (43), 23634–23645. https://doi.org/10.1021/acs.jpcc.1c07597.

(26) Lerner, E.; Cordes, T.; Ingargiola, A.; Alhadid, Y.; Chung, S.; Michalet, X.; Weiss, S. Toward Dynamic Structural Biology: Two Decades of Single-Molecule Förster Resonance Energy Transfer. *Science* **2018**, *359* (6373), eaan1133. https://doi.org/10.1126/science.aan1133.

(27) Yang, H.; Luo, G.; Karnchanaphanurach, P.; Louie, T.-M.; Rech, I.; Cova, S.; Xun, L.; Xie, X. S. Protein Conformational Dynamics Probed by Single-Molecule Electron Transfer. *Science* **2003**, *302* (5643), 262–266. https://doi.org/10.1126/science.1086911.

(28) Lu, H. P.; Xun, L.; Xie, X. S. Single-Molecule Enzymatic Dynamics. *Science* **1998**, *282* (5395), 1877–1882. https://doi.org/10.1126/science.282.5395.1877.

(29) Levi, V.; Ruan, Q.; Gratton, E. 3-D Particle Tracking in a Two-Photon Microscope: Application to the Study of Molecular Dynamics in Cells. *Biophys. J.* **2005**, *88* (4), 2919–2928. https://doi.org/10.1529/biophysj.104.044230.

(30) Hou, S.; Welsher, K. An Adaptive Real-Time 3D Single Particle Tracking Method for Monitoring Viral First Contacts. *Small* **2019**, *15* (44), 1903039. https://doi.org/10.1002/smll.201903039.

(31) Wells, N. P.; Lessard, G. A.; Goodwin, P. M.; Phipps, M. E.; Cutler, P. J.; Lidke, D. S.; Wilson, B. S.; Werner, J. H. Time-Resolved Three-Dimensional Molecular Tracking in Live Cells. *Nano Lett.* **2010**, *10* (11), 4732–4737. https://doi.org/10.1021/nl103247v.

(32) Gahlmann, A.; Moerner, W. E. Exploring Bacterial Cell Biology with Single-Molecule Tracking and Super-Resolution Imaging. *Nat. Rev. Microbiol.* **2014**, *12* (1), 9–22. https://doi.org/10.1038/nrmicro3154.

(33) Schuster, B. S.; Ensign, L. M.; Allan, D. B.; Suk, J. S.; Hanes, J. Particle Tracking in Drug and Gene Delivery Research: State-of-the-Art Applications and Methods. *Adv. Drug Deliv. Rev.* **2015**, *91*, 70–91. https://doi.org/10.1016/j.addr.2015.03.017.

(34) Patterson, G.; Davidson, M.; Manley, S.; Lippincott-Schwartz, J. Superresolution Imaging Using Single-Molecule Localization. *Annu. Rev. Phys. Chem.* **2010**, *61* (1), 345–367. https://doi.org/10.1146/annurev.physchem.012809.103444.

(35) Huang, B.; Babcock, H.; Zhuang, X. Breaking the Diffraction Barrier: Super-Resolution Imaging of Cells. *Cell* **2010**, *143* (7), 1047–1058. https://doi.org/10.1016/j.cell.2010.12.002.

(36) Rust, M. J.; Bates, M.; Zhuang, X. Sub-Diffraction-Limit Imaging by Stochastic Optical Reconstruction Microscopy (STORM). *Nat. Methods* **2006**, *3* (10), 793–796. https://doi.org/10.1038/nmeth929.

(37) Schnitzbauer, J.; Strauss, M. T.; Schlichthaerle, T.; Schueder, F.; Jungmann, R. Super-Resolution Microscopy with DNA-PAINT. *Nat. Protoc.* **2017**, *12* (6), 1198–1228. https://doi.org/10.1038/nprot.2017.024.

(38) Blythe, K. L.; Willets, K. A. Super-Resolution Imaging of Fluorophore-Labeled DNA Bound to Gold Nanoparticles: A Single-Molecule, Single-

Particle Approach. *J. Phys. Chem. C* **2016**, *120* (2), 803–815. https://doi.org/10.1021/acs.jpcc.5b08534.

(39) Biteen, J. S.; Thompson, M. A.; Tselentis, N. K.; Bowman, G. R.; Shapiro, L.; Moerner, W. E. Super-Resolution Imaging in Live Caulobacter Crescentus Cells Using Photoswitchable EYFP. *Nat. Methods* **2008**, *5* (11), 947–949. https://doi.org/10.1038/nmeth.1258.

(40) Gordon, M. P.; Ha, T.; Selvin, P. R. Single-Molecule High-Resolution Imaging with Photobleaching. *Proc. Natl. Acad. Sci.* **2004**, *101* (17), 6462–6465. https://doi.org/10.1073/pnas.0401638101.

(41) Lidke, K. A.; Rieger, B.; Jovin, T. M.; Heintzmann, R. Superresolution by Localization of Quantum Dots Using Blinking Statistics. *Opt. Express* **2005**, *13* (18), 7052–7062. https://doi.org/10.1364/OPEX.13.007052.

(42) Qu, X.; Wu, D.; Mets, L.; Scherer, N. F. Nanometer-Localized Multiple Single-Molecule Fluorescence Microscopy. *Proc. Natl. Acad. Sci.* **2004**, *101* (31), 11298–11303. https://doi.org/10.1073/pnas.0402155101.

(43) Bates, M.; Huang, B.; Dempsey, G. T.; Zhuang, X. Multicolor Super-Resolution Imaging with Photo-Switchable Fluorescent Probes. *Science* **2007**, *317* (5845), 1749–1753. https://doi.org/10.1126/science.1146598.

(44) Wijesooriya, C. S.; Peterson, J. A.; Shrestha, P.; Gehrmann, E. J.; Winter, A. H.; Smith, E. A. A Photoactivatable BODIPY Probe for Localization-Based Super-Resolution Cellular Imaging. *Angew. Chem.* **2018**, *130* (39), 12867–12871. https://doi.org/10.1002/ange.201805827.

(45) Introduction: Super-Resolution and Single-Molecule Imaging. *Chem. Rev.* **2017**, *117* (11), 7241–7243. https://doi.org/10.1021/acs.chemrev.7b00242.

(46) Hell, S. W. Nanoscopy with Focused Light (Nobel Lecture). *Angew. Chem. Int. Ed.* **2015**, *54* (28), 8054–8066. https://doi.org/10.1002/anie.201504181.

(47) Hell, S. W. Far-Field Optical Nanoscopy. *Science* **2007**, *316* (5828), 1153–1158. https://doi.org/10.1126/science.1137395.

(48) Sieber, J. J.; Willig, K. I.; Heintzmann, R.; Hell, S. W.; Lang, T. The SNARE Motif Is Essential for the Formation of Syntaxin Clusters in the Plasma Membrane. *Biophys. J.* **2006**, *90* (8), 2843–2851. https://doi.org/10.1529/biophysj.105.079574.

(49) Donnert, G.; Keller, J.; Wurm, C. A.; Rizzoli, S. O.; Westphal, V.; Schönle, A.; Jahn, R.; Jakobs, S.; Eggeling, C.; Hell, S. W. Two-Color Far-Field Fluorescence Nanoscopy. *Biophys. J.* **2007**, *92* (8), L67–L69. https://doi.org/10.1529/biophysj.107.104497.

(50) Willig, K. I.; Rizzoli, S. O.; Westphal, V.; Jahn, R.; Hell, S. W. STED Microscopy Reveals That Synaptotagmin Remains Clustered after Synaptic Vesicle Exocytosis. *Nature* **2006**, *440* (7086), 935–939. https://doi.org/10.1038/nature04592.

(51) Lelek, M.; Gyparaki, M. T.; Beliu, G.; Schueder, F.; Griffié, J.; Manley, S.; Jungmann, R.; Sauer, M.; Lakadamyali, M.; Zimmer, C. Single-Molecule Localization Microscopy. *Nat. Rev. Methods Primer* **2021**, *1* (1), 1–27. https://doi.org/10.1038/s43586-021-00038-x.

(52) Betzig, E.; Patterson, G. H.; Sougrat, R.; Lindwasser, O. W.; Olenych, S.; Bonifacino, J. S.; Davidson, M. W.; Lippincott-Schwartz, J.; Hess, H. F. Imaging Intracellular Fluorescent Proteins at Nanometer Resolution. *Science* **2006**, *313* (5793), 1642–1645. https://doi.org/10.1126/science.1127344.

(53) Shashkova, S.; Leake, M. C. Single-Molecule Fluorescence Microscopy Review: Shedding New Light on Old Problems. *Biosci. Rep.* **2017**, *37* (4), BSR20170031. https://doi.org/10.1042/BSR20170031.

(54) Huang, T.; Phelps, C.; Wang, J.; Lin, L.-J.; Bittel, A.; Scott, Z.; Jacques, S.; Gibbs, S. L.; Gray, J. W.; Nan, X. Simultaneous Multicolor Single-Molecule Tracking with Single-Laser Excitation via Spectral Imaging. *Biophys. J.* **2018**, *114* (2), 301–310. https://doi.org/10.1016/j.bpj.2017.11.013.

(55) Valley, C. C.; Liu, S.; Lidke, D. S.; Lidke, K. A. Sequential Superresolution Imaging of Multiple Targets Using a Single Fluorophore. *PLOS ONE* **2015**, *10* (4), e0123941. https://doi.org/10.1371/journal.pone.0123941.

(56) Tam, J.; Cordier, G. A.; Borbely, J. S.; Álvarez, Á. S.; Lakadamyali, M. Cross-Talk-Free Multi-Color STORM Imaging Using a Single Fluorophore. *PLOS ONE* **2014**, *9* (7), e101772. https://doi.org/10.1371/journal.pone.0101772.

(57) Wade, O. K.; Woehrstein, J. B.; Nickels, P. C.; Strauss, S.; Stehr, F.; Stein, J.; Schueder, F.; Strauss, M. T.; Ganji, M.; Schnitzbauer, J.; Grabmayr, H.; Yin, P.; Schwille, P.; Jungmann, R. 124-Color Super-Resolution Imaging by Engineering DNA-PAINT Blinking Kinetics. *Nano Lett.* **2019**, *19* (4), 2641–2646. https://doi.org/10.1021/acs.nanolett.9b00508.

(58) Lubeck, E.; Cai, L. Single-Cell Systems Biology by Super-Resolution Imaging and Combinatorial Labeling. *Nat. Methods* **2012**, *9* (7), 743–748. https://doi.org/10.1038/nmeth.2069.

(59) Grußmayer, K. S.; Geissbuehler, S.; Descloux, A.; Lukes, T.; Leutenegger, M.; Radenovic, A.; Lasser, T. Spectral Cross-Cumulants for Multicolor Super-Resolved SOFI Imaging. *Nat. Commun.* **2020**, *11* (1), 3023. https://doi.org/10.1038/s41467-020-16841-1.

(60) Clowsley, A. H.; Kaufhold, W. T.; Lutz, T.; Meletiou, A.; Di Michele, L.; Soeller, C. Repeat DNA-PAINT Suppresses Background and Non-Specific Signals in Optical Nanoscopy. *Nat. Commun.* **2021**, *12* (1), 501. https://doi.org/10.1038/s41467-020-20686-z.

(61) Wustholz, K. L.; Bott, E. D.; Kahr, B.; Reid, P. J. Memory and Spectral Diffusion in Single-Molecule Emission. *J. Phys. Chem. C* **2008**, *112* (21), 7877–7885. https://doi.org/10.1021/jp711687j.

(62) Watkins, L. P.; Yang, H. Detection of Intensity Change Points in Time-Resolved Single-Molecule Measurements. *J. Phys. Chem. B* **2005**, *109* (1), 617–628. https://doi.org/10.1021/jp0467548.

Chapter II: Blinking-Based Multiplexing for Classifying Spectrally-Overlapped Emitters

2.1 Introduction

Optical imaging of biological systems is a powerful tool for visualizing nanoscale structures. With greater insight into these structures, such as proteins, organelles, or even entire cells, we can better understand their functions and purposes in the body as well as their complex and dynamic interactions with other elements of the system.[1,2] Such insights allow for deeper knowledge of the origin of disease states and possible treatments for the cure or prevention of illness. Although imaging can be performed with conventional light microscopy, these experiments suffer from poor sensitivity and resolution due to the diffraction limit of light.[3,4] Over the 20th century, however, significant advancements and developments in microscope, detector, and laser technology have ameliorated these issues. The emergence of single-molecule spectroscopy (SMS) highlights the enhanced sensitivity of modern instruments, as these studies allow for the detection of emission from just one molecule at a time. Additionally, SMS has led to the discovery of unusual photophysical phenomena such as blinking. Defined as the random fluctuations in emissive intensity of a single emitter under continuous laser excitation, blinking has made substantial impacts on the advancement of fluorescence imaging.

Until recently, blinking has been most commonly exploited for two key purposes: (1) to report on heterogeneities in the local environment and (2) to localize the precise position of individual emitters. The former is often referred to as

"nanoreporting" because molecules' behavior, which is dependent on the local environment, is manifested through their blinking dynamics. Probing the behavior of individual fluorophores informs upon heterogeneities and changes that would otherwise be hidden in a bulk measurement. For instance, blinking experiments have been used to study protein folding, electron transfer dynamics, and nanophotonics.[5–9] The latter use of blinking, localization, has significant applications in imaging, as it is utilized heavily in super-resolution imaging (SRI) techniques such as stochastic optical reconstruction microscopy (STORM).[10] These techniques allow researchers to move beyond the diffraction limit and probe nanoscale systems with unprecedented spatial resolution.[11,12] In STORM, individual emitters are localized through the detection of their stochastic emission. Blinking is essential here because it ensures that only a subset of isolated emitters fluoresce at once, allowing for accurate localization.

Currently, multicolor imaging relies on measuring spectral color to distinguish emission signals. To limit the misidentification of emitters due to overlapping fluorescence signal, an issue called spectral crosstalk, the selected probes must have distinct emission spectra (i.e., separation of at least 50-100 nm).[13] Consequently, there are few combinations of compatible, high-performance probes that can be used together in an imaging experiment. To circumvent the complications of crosstalk, multicolor images are often created using sequential imaging. Localizing emitters one class at a time accommodates for any differences in experimental conditions that may hinder simultaneous data collection (e.g., solvent, excitation power, or excitation wavelength) and ensures more accurate results. Unfortunately, this stepwise method also adds

significantly to the time and complexity of an experiment. With these challenges in mind, the Wustholz group sought to use its expertise in blinking experiments to develop simpler means for distinguishing emitters.

In 2022, we pushed beyond the boundaries of traditional blinking experiments by proposing a third use for blinking: emitter identification in multicolor imaging.[14] Blinking-based multiplexing (BBM) eliminates the experimental demands of sequential imaging by facilitating automated differentiation of spectrally-overlapped emitters with just one excitation source (**Figure 1**). Since spectrally-overlapped probes absorb and emit at similar wavelengths, the emitters cannot be distinguished via their emission color.
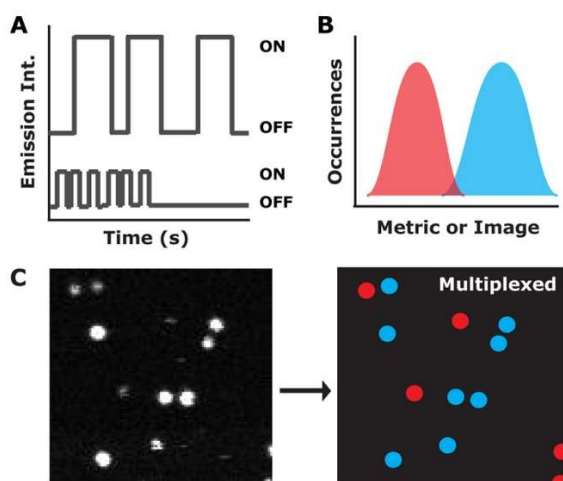
Figure 1. BBM concept. (A) Two classes of spectrally overlapped emitters exhibit distinct blinking behavior. (B) The distributions of this behavior are quantified to develop a metric for classification. (C) The original emission image can be color coded according to the results of metric analysis.

However, the Wustholz group, with over a decade of studying single-molecule blinking, observed qualitative dissimilarities in the blinking traces of spectrally-overlapped fluorophores. BBM exploits these differences in the intrinsic blinking behavior of various emitters to overcome the limitations of current multicolor imaging techniques.

BBM does not require that emitters are spectrally separated, but it does require that their blinking dynamics are distinct. To demonstrate the principle of BBM,

rhodamine 6G (R6G), an organic dye, and core-shell CdSe/ZnS quantum dots (QD), a type of semiconductor nanoparticle, are selected as the initial emitter system. These two emitters are an optimal choice for initial BBM proof-of-concept because they are
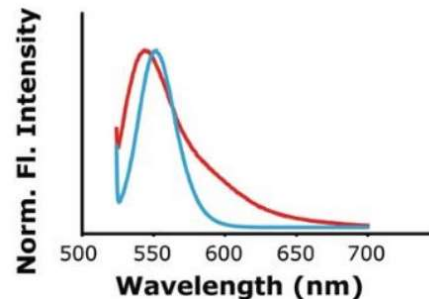
Figure 2. Emission spectra of QD and R6G are significantly overlapped.

commercially available, spectrally overlapped (**Figure 2**), and known to exhibit different photophysical mechanisms for blinking.[15,16] In this chapter, the development, testing, and refinement of the BBM method are described for R6G and QD on glass before moving on to test BBM in more complex systems in Chapter 3.

2.2 Methods

2.2.1 Materials and Sample Preparation

R6G (Acros Organics, 99%) and QD (Invitrogen, Qdot 565 ITK carboxyl quantum dots, 8 μM solution in borate buffer) were used as received. All glassware was cleaned in a base bath (~1 M KOH) for 12-24 h and rinsed with ultrapure water (ThermoScientific, EasyPure II, 18.2 MΩ cm). Microscope coverslips (Fisher Scientific, 12-545-102) were base bathed for 12-24 h, rinsed with ultrapure water, and dried with clean air (Wilkerson, X06-02-000). Stock solutions were prepared in ultrapure water and sonicated for 1-2 min before use. QD and R6G stock solutions were diluted stepwise to ~1 nM concentrations to achieve appropriate labeling densities for single-molecule studies. Samples were prepared by spin coating 35 μL of the resulting

solution onto a clean glass coverslip using a spin coater (Laurell Technologies, WS-400-6NPP-LITE) operating at 3000 rpm with a 5 s acceleration time and a 30 s spin time.

2.2.2 Single-Molecule Spectroscopy and Data Analysis

For single-molecule experiments, samples were mounted onto a custom aluminum flow cell (approximately 1.5" × 3" × 0.5", equipped with Tygon tubing) and flushed with dry nitrogen gas (Airgas, 100%). The secured flow cell was placed on a nanopositioning stage (Physik Instrument, LP E545) atop an inverted confocal microscope (Nikon, TiU). A high numerical aperture (NA) 100x oil-immersion objective (Nikon Plan Fluor, NA = 1.3) focused laser excitation at 532 nm (Spectra Physics, Excelsior) to a diffraction limited spot. An excitation power (P_{exc}) of 1.05 μW was used for single-emitter measurements of both R6G and QD to maximize emission signal while limiting photobleaching. Emission from the sample was collected through the objective and passed through an edge filter (Semrock, LP03-532RS-2S) before being focused to an avalanche photodiode detector (APD) with a 50 μm aperture (MPD, PDM050CTB) to achieve confocal resolution. Focus during raster scans was maintained using a z-axis microscope lock (Applied Science Instruments, MFC-2000). A custom LabView program was used to control the nanopositioning stage and collect corresponding emission intensities using a 30 ms dwell time. Single emitters were identified on the observation of blinking dynamics, diffraction-limited spots,

irreversible molecular photobleaching, and concentration dependence of spot density. All blinking traces were collected over 200 s with a 10 ms bin time (t_{bin}).

Blinking traces were analyzed using the change point detection (CPD) method (MATLAB 2022). CPD uses generalized likelihood tests to determine the statistically significant intensity levels of each trace and their corresponding temporal durations. The lowest deconvolved intensity level is defined as nonemissive (off), and intensity levels that are greater than one standard deviation above the root-mean-square noise are defined as emissive (on). An interval refers to the entire duration of time that a blinking trace is above or below this threshold (i.e., on and off intervals, respectively). Within these larger intervals, there may be successive changes in intensity level that do not signify a switch between on and off, which are called segments. For each blinking trace, CPD outputs fourteen blinking statistics that relate to these analytically determined intensity levels, intervals, segments, and durations.

2.3   Results and Discussion

2.3.1 Blinking Dynamics of QD and R6G on Glass

Blinking traces of 143 QD and 148 R6G were collected on a confocal microscope at P_{exc} = 1 μW with t_{bin} = 10 ms. Consistent with previous single-molecule studies, the two classes of emitters display, on average, visually distinct behavior (**Figure 3A-B**).[16,17] To analyze each blinking trace, CPD is used. Histograms of the resulting statistics reveal the distributions for each emitter. For example, on average, QD display more unique intensity levels (N_I), higher segment event frequencies (ν_E),

and higher dispersion in both statistics than R6G, as shown in **Figure 3C-D**. Although these distributions display some degree of separation for the two emitters, neither statistic alone is sufficient to distinguish between them in the case of an unknown emitter. Consequently, a combined metric must be used for classification.

The differences in QD and

Figure 3. BBM with R6G (red) and QD (blue). Representative blinking traces of (A) R6G and (B) QD on glass display qualitative differences. The structures of each emitter are displayed above their respective traces. Distributions for (C) N_I and (D) ν_E for the emitters are overlapped, but, on average QD dynamics yield higher values and greater dispersion than R6G.

R6G behavior can be attributed to their distinct photophysical blinking mechanisms. Previous work attributes dark states of R6G on glass to intersystem crossing to the first triplet state (T[1]).[18] However, more recently, R6G blinking has been found to be due electron transfer (ET) to charge trap states on the glass surface, meaning that an excited molecule may donate an electron to a nearby vacancy on the substrate.[19] The on and off time distributions of R6G have been shown to be lognormal, which is consistent with the Albery model for complex ET.[17,20,21] The Albery model describes the activation barriers to ET as a Gaussian distribution such that:

$$\Delta G^{\ddagger} = \Delta G_0^{\ddagger} + \gamma x RT \tag{1}$$

where $\Delta G_0^{\ddagger}$ is the mean activation barrier, γ is the extent of energetic dispersion about $\Delta G_0^{\ddagger}$, and x is a random number generated from a Gaussian distribution. When

28

Equation 1 is substituted into the Arrhenius equation, the following rate constant (k_{ij})

expression results:

$$k_{ij} = \kappa_{ij}e^{-\gamma x} \tag{2}$$

with i and j representing the initial and final states of ET, respectively, and κ_{ij} being a

first-order rate constant corresponding to the mean activation barrier. Because

activation barriers are assumed to be normally distributed according to the Albery

model, the rate constants of ET and their corresponding on and off times are

lognormally distributed.

The exact cause of fluorescence intermittency in QDs is a subject of active

inquiry, but two proposed mechanisms are thought to dominate: Type I (charging

model) and Type II blinking.[22] Type I blinking is a result of the charging and

subsequent neutralization of the nanocrystal core. Essentially, excitation induces a

charge-hole pair, or exciton, and one charge can be photoionized into a dark trap state

on the nanocrystal surface, leaving the QD core temporarily charged.[23] At this point,

the QD may still promote additional electrons to the conduction band, but a fast process

called Auger recombination prevents radiative release of energy. Auger recombination

refers to the non-radiative transfer of energy from the new exciton to the remaining

charge in the nanoparticle core. Once the electron-hole pair recombines, the system is

neutralized, and the QD becomes fluorescent once again. According to this model, the

length of a dark state depends on the lifetime of the charge trap, which suggests long

durations for trap states. Type II blinking is dictated by fluctuations in the rate of charge

trapping on the QD surface. In this model, fluorescence is interrupted when a positive

hole charge from an exciton gets transferred to a dark trap state, and it quickly recombines non-radiatively with the promoted electron to neutralize the nanocrystal core before the next exciton is created.[22] This process only takes place when the hole trapping rate is larger than the fluorescence recombination rate, as the emitter will remain fluorescent when recombination occurs on a faster timescale than trapping. Trapping rate is proposed to vary over time due to gradual changes in the number of active, available trap sites on the QD surface. Unlike the charging model, Type II blinking does not require long-lived trap states but rather periods of time where trapping occurs faster than radiative recombination. Experimental results suggest that both the Type I and Type II mechanisms contribute to QD blinking.

2.3.2 Metric-Based Blinking-Based Multiplexing

As a first step toward classification of QD and R6G, BBM is executed using an empirically-derived mathematical metric.[14] Analyzing histograms of the fourteen CPD-derived blinking statistics (e.g., **Figure 3C-D**) reveals that the following five statistics have the best separation for these two emitters: number of unique intensity levels (N_I), minimum emissive intensity (I_{min}), segment event frequency (ν_E), average intensity ($\langle I \rangle_t$), and average on interval time ($\langle t_{on} \rangle$). The metric value (*M*) for each individual probe is calculated using the following equation:

$$M = N_I I_{min} \nu_E{}^2 \langle I \rangle^2 \langle t_{on} \rangle \tag{3}$$

For each of the included blinking statistics, the distribution of values for QD is, on average, higher than those for R6G. Multiplying these key statistics together

exaggerates distributional differences between the emitters, thus allowing for more accurate classification. Several alternative metrics were tested before settling on **Equation 3**, which maximizes classification accuracy while minimizing errors. Before calculating M for each emitter, the data is normalized to the entire dataset of known R6G and QD emitters (n = 291) and multiplied by 100. Normalization ensures that each statistic is weighted equally, and multiplication prevents M values from being < 1. **Figure 4A** reveals that the distribution of M values for R6G and QD are relatively well separated.

To assess the ability of **Equation 3** to distinguish QD and R6G, receiver operating characteristic (ROC) curve analysis is performed. ROC curves, often used in chemical sensing and clinical diagnostics, reveal the success of a classifying metric by visualizing the true positive rate (TPR) and false positive rate (FPR) as the threshold for binary classification is altered.[24,25] A true positive occurs when an actually positive data point is correctly predicted as such, and TPR can be calculated as $TPR = \frac{TP}{TP+FN}$. A false positive refers to an actually false data point being incorrectly predicted as true,
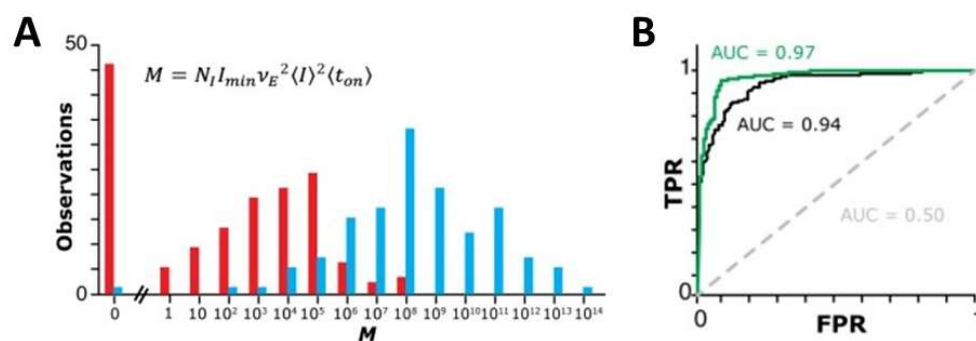
Figure 4. (A) Histogram of M values for R6G (red) and QD (blue). (B) ROC curves for R6G/QD classification based on M (green), ν_E (black), and random guessing (dashed).

and FPR can be calculated as FPR=$\frac{FP}{FP+TN}$. The abbreviations TP, FP, TN, and FN correspond to true positives, false positives, true negatives, and false negatives, respectively. Perfect classification yields a point at (0,1), which indicates that all points are correctly identified with no errors. To the opposite effect, random guessing yields a diagonal that bisects the ROC space. The area under the curve (AUC) is dictated by the shape of the graph and demonstrates the metric's performance, with values closer to 1 indicating better classification. The first example would result in AUC = 1, revealing flawless classification, whereas the latter case would have AUC = 0.5. For this study, a true positive is defined as R6G, whereas a true negative corresponds to QD. **Figure 4B** shows ROC curves regarding the classification of QD and R6G based on M, ν_E, and random guessing. Although basing classification on ν_E alone demonstrates promise (AUC = 0.94), M is the superior metric (AUC = 0.97).

In addition to assessing the performance of various metrics, ROC curve analysis can be used to establish a numerical cutoff for binary classification of R6G and QD. The shape of the curve reveals the point that maximizes TPR and minimizes FPR. By analyzing the ROC curve for M, a cutoff between 3.7×10^4 and 8.25×10^5 is determined to achieve that goal. However, significant overlap in the middle of the distribution ($3.7 \times 10^4 < M < 8.25 \times 10^5$) prevents accurate emitter classification in that region. Consequently, we apply a double threshold, where emitters with $M > 8.25 \times 10^5$ were classified as QDs, and those with $M < 3.7 \times 10^4$ were classified as R6G. When applied to the entire dataset of emitters, M classifies R6G and QD with 93.5% (272/291) accuracy. Although this result demonstrates excellent BBM

performance, the double threshold approach excludes ~8% of data by omitting emitters with M values that fall in the unclassified middle region.

To account for the excluded data points, we implement a second classification metric. In collecting blinking traces of R6G and QD, experimentalists recognized qualitative distinctions between their emissive behavior to the extent where emitters could be accurately classified through visual observation. A simple, yet effective manner for discriminating QD from R6G is the duration of emissive activity. Whereas QD demonstrates blinking throughout the 200 s period, R6G often photobleaches early on (i.e., it undergoes an irreversible photochemical change that no longer allows it to be excited by the wavelength of the laser source or fluoresce). Therefore, we introduce the secondary metric called "blinking past 150 seconds" for emitters that fail to be categorized by M. Unknown emitters that display emissive activity 150 seconds or later in the 200 s blinking trace are categorized as QD, and those that do not are marked as R6G. Adding on this blinking stipulation lowers the overall classification accuracy slightly to 92.5%, only a small tradeoff to make in exchange for inclusion of the full dataset (n = 291) in analysis.

Next, BBM performance is tested by applying the dual metric system to mixed samples of QD and R6G. Blinking traces were collected from three mixtures of known composition—30:70 (n = 109), 50:50 (n = 145), and 70:30 (n = 97) QD to R6G by concentration— and analyzed using CPD and BBM metrics, as previously described. If the BBM model performs well for this given system, the metrics would predict a 30/70, 50/50, and 70/30 split of QD and R6G, respectively.

The results of BBM analysis on each mixed emitter sample are presented in **Table 1**. There is excellent agreement between the expected composition, as determined by the ratio of concentrations, and the predicted composition. Small deviations from the expected values are attributed to sampling error, as caused by the limited size of the datasets (n = 109, 145, and 97, respectively). Even so, in each case, predictions fall within 5% (and as low as just 1%) of the expected value, further demonstrating the strong performance of the BBM model in this proof-of-concept study.

[QD] : [R6G]	
Expected	**Predicted**
30 : 70	33.9 : 66.1
50 : 50	51.0 : 49.0
70 : 30	74.2 : 25.8

Table 1. Expected composition of QD:R6G by concentration, compared to the composition as predicted by BBM.

2.3.3 Machine Learning-Based Blinking-Based Multiplexing

Despite high (92.5%) accuracy using *M*-based BBM, this approach was catered to the specific blinking properties of QD and R6G emitters. Therefore, the scope of this method is limited, as *M* does not necessarily capture the differences in blinking dynamics of other fluorophores, such as other rhodamine derivative dyes. Furthermore, *M* was optimized to QD and R6G blinking specifically on a glass substrate at P_{exc} = 1.05 μW and t_{bin} = 10 ms, so it does not account for changes in blinking dynamics that may be induced by alterations to experimental conditions. In addition, it took experimentalists upwards of two weeks to generate a metric for this simple binary system. In future endeavors, faster analysis and model building would allow for more

efficient experimental execution and more rapid BBM results. For these reasons, the future of BBM has shifted towards machine learning techniques such as deep learning (DL) and logistic regression (LR), which can rapidly generate predictive models for classification of any system of emitters under any experimental conditions.[26–28]

2.3.3.1 Deep Learning

First, DL is explored as an alternative to *M*-based analysis. Using a one-dimensional counterpart of residual neural network model with 13 convolutional layers and 1 dense layer, DL analysis on the previously described datasets of 143 QD and 148 R6G molecules achieved an average classification accuracy of 93.2% and a maximum accuracy of 96.6%. Furthermore, when applied to the mixed emitter datasets of expected compositions 30:70, 50:50, and 70:30 QD to R6G, the average predicted compositions are 34.4:65.6, 42.1:57.9, and 60.8:39.4, respectively. Although within 10% of the expected compositions, these results are not as accurate as what is achieved through CPD and metric analysis. Once again, deviations are expected due to the small size of the acquired datasets, but this error emphasizes some of the major shortcomings of DL. DL requires incredibly large datasets for training models and is computationally expensive.[27] Additionally, DL utilizes hard classification in its predictions, meaning the model assigns each data point a definitive class rather than reporting probabilities for classification in each group.

2.3.3.2 Logistic Regression

Given the limitations of DL for BBM, an alternative machine learning technique the lab investigated is LR. LR has the capability to quickly generate accurate soft classification models without large datasets or considerable computational expense.[26,29–31] LR classifies binary or higher order systems by using maximum likelihood estimation to fit the system to a sigmoid, or logistic, function. The resulting model gives the probability of a single emitter to belong to class A (P_A) as a function of an input predictor (x):

$$P_A(x) = [1 + e^{-(mx+b)}]^{-1} \tag{4}$$

where m and b are the regression coefficient and y-intercept fit parameters, respectively. Here, x is a single CPD-derived blinking statistic. LR generates the model by plotting the blinking statistic values against binary probabilities; for example, a known QD would be given the value $P_{QD} = 1$ and a known R6G would have value $P_{QD} = 0$. LR then fits the data to a sigmoid by determining appropriate fit parameters.

A sample classification using LR is shown in **Figure 5A**. As seen in *M*-based BBM, N_I for QD is higher, on average, than for R6G. To be specific, QD has an average value, $\langle N_I \rangle$, of 17.1 ± 0.6 whereas R6G has $\langle N_I \rangle$ of 6.0 ± 0.3. If N_I is used as the only input, LR generates a model with $b = -5.2$ and $m = 0.5$. Plugging these values into **Equation 4**, we now have a function that can predict the identity of individual data points. For instance, an unknown emitter with $N_I = 12$ results in $P_{QD} = 0.69$. For a binary system, the default classification threshold is 0.50, so this emitter would be classified as QD. Despite overlap in the N_I distributions for QD and R6G, LR with this

single blinking statistic yields an overall classification accuracy of 85.9%. As previously discovered in *M*-based analysis, however, identification accuracy is improved by incorporating more than one CPD-derived statistic into classification.

A major advantage of LR is its adaptability. As will be further explored in Chapter 3, LR can be applied to any emitter system under any experimental condition, and it can also generate models with multiple input variables (called multinomial LR). Multinomial LR works similarly to its binomial counterpart except that it takes in several independent input predictors $(x, y, …)$ to generate a multidimensional sigmoid as follows:

$$P_A(x, y, …) = \left[1 + e^{-(mx+ny\ …b)}\right]^{-1} \tag{5}$$

where the fit parameters are b and the regression coefficients $(m, n, …)$, which correspond to each predictor $(x, y, …)$, respectively. These inputs must be standardized because interpretation is difficult and ineffective without a common scale. Standardization occurs via the *z*-score normalization approach. For each blinking trace, $z = \frac{(x - \mu)}{\sigma}$ is calculated, where μ is the mean of the blinking statistic and σ is its standard deviation for the entire dataset. For the purpose of BBM, 10 independent CPD-derived blinking statistics are used as input predictors: N_I, I_{min}, I_{max}, $\langle I \rangle_t$, $\langle t_{on,int} \rangle$, $\langle t_{off,int} \rangle$, $\langle t_{on,seg} \rangle$, $\langle t_{off,seg} \rangle$, $N_{on,seg}$, and $N_{off,seg}$. The remaining 4 CPD statistics are excluded due to high correlation with one or more of the 10 included values; for instance, switching frequencies are directly related to the number of segments and

intervals in a given blinking trace. Reducing collinearity eliminates redundancy in the logistic model and, in effect, allows for more reliable interpretation of regression coefficients.[26]

With the desired input predictors decided, LR is applied to the 291 QD and R6G emitters on glass at $P_{exc} = 1$ µW to give the following best fit logistic model in the form $P_{QD} = [1 + e^{-z}]^{-1}$, where

$$z = 8.5 I_{min} + 4.0 N_I - 3.8 I_{max} + 3.2 \langle I \rangle_t - 3.0 \langle t_{off,seg} \rangle + 1.2 \langle t_{off,int} \rangle$$

$$+ 0.7 N_{off,seg} + 0.6 \langle t_{on,int} \rangle - 0.1 N_{on,seg} + 0.04 \langle t_{on,seg} \rangle + 2.2$$

$$(6)$$

with regression coefficients listed in descending order. The magnitude of the coefficients signifies the importance of the corresponding blinking statistic in discriminating the two emitters. In other words, because of their comparatively large coefficients, I_{min}, N_I, I_{max}, and $\langle I \rangle_t$ have the biggest influence over classification, which indicates that intensities are key for distinguishing between R6G and QD. On the other hand, $\langle t_{on,seg} \rangle$ and $N_{on,seg}$ have coefficients that are close to zero, meaning that the number and durations of on segments have little impact on classification. With this model and a default binary classification threshold (i.e., P_{QD} or $P_{R6G} > 0.5$ for an emitter results in classification as QD or R6G, respectively), 92.7% (270/291) of QD and R6G emitters are correctly classified. In just a minute or less, LR generates a high-performance model that can classify emitters with an accuracy that rivals that of the empirically-derived metric (which had 92.5% accuracy).

Accuracy alone does not explain the whole story. To gain greater insight into
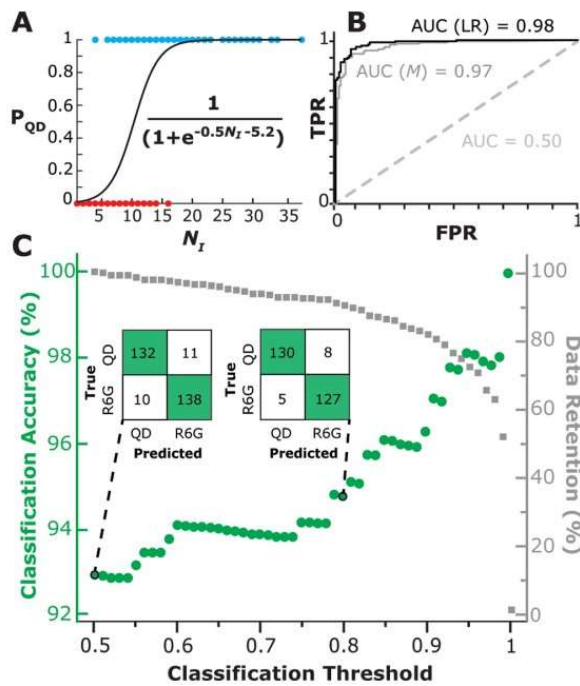
Figure 5. (A) LR-derived model for classification of QD and R6G on glass at P_{exc} = 1 µW and t_{bin} = 10 ms using N_I as the only input predictor yields 85.9% classification accuracy. (B) ROC plots of multinomial LR-based classification (black) and M-based classification (gray) have AUC = 0.98 and 0.97, respectively, revealing the superior performance of LR. (C) Overall classification accuracy of LR (green) improves as the classification threshold is increased from 0.5 to 1 and less certain data is omitted. Inset confusion matrices at thresholds 0.5 and 0.8 offer greater detail into LR performance at each point. Data retention (gray) reveals the balance between accuracy and data inclusion.

the performance of the LR model, we once again use ROC curve analysis to uncover the TPR and FPR of the system. The same methodology as described above was used to create a ROC curve corresponding to LR classification, where the LR probability outputs are thresholded to generate the plot. The resulting graph and the M-based curve are overlaid in **Figure 5B**. High AUC values of 0.97 and 0.98 for M-based and LR-based classification indicate that both methods display exceptional performance in classifying this system, but LR has a slight advantage. Between its rapid, automated, and accurate model generation, its superior AUC value, and its use of soft classification, LR is the clear choice for BBM analysis.

As revealed by the ROC curve, the classification threshold can be adjusted from the default for a binary system (i.e., P_A > 0.5 leads to classification in class A) to maximize TPR and minimize FPR. **Figure 5C** demonstrates how TPR, FPR, and

overall classification accuracy are affected as the threshold is varied. As mentioned, in the default case, LR correctly classifies 270/290 (92.7%) of R6G and QD emitters. From the inset confusion matrices, the number of TP, TN, FP, and FN emitters are identified to calculate TPR = 132/143 (0.92) and FPR = 10/148 (0.07). As a reminder, QD is defined as "positive" and R6G is defined as "negative." When the classification threshold is increased to 0.8, the overall accuracy increases to 257/270 (94.8%) correctly classified emitters. In this case, P_{QD} or $P_{R6G} > 0.8$ are classified as QD or R6G, respectively, and the "less certain" emitters that fall below this threshold are omitted from analysis. At this new threshold, TPR = 0.94 and FPR = 0.04. The increase in TPR and overall accuracy and the decrease in FPR are improvements over default classification.

Classification thresholding, unfortunately, comes at a small cost. Because emitters that fall below the altered threshold cannot be classified, they must be discarded. However, note that in the example described above, shifting the classification threshold from 0.5 to 0.8 leads to the exclusion of only 21 emitters (7.2% of the total dataset of 291 QD and R6G). **Figure 5C** visualizes the balance between overall accuracy and data retention as classification threshold is varied. The threshold can be tuned accordingly depending on the application. In data-dense experiments such as SRI, classification accuracy may be valued over data retention, and an accuracy of ~98% can be reached by discarding only ~25% of emitters. A further consideration is that the shape of this graph changes based on the emitter system, sample size, and experimental conditions, so the abrupt increases and decreases in accuracy that are seen

here may be smoothed in the case of a larger dataset. With or without applying a classification threshold, the improved accuracy of LR indicates its superiority over metric-based classification.

To demonstrate the generalizability of multinomial LR as compared to *M*-based classification, both methods are applied to new datasets of QD and R6G collected at decreased and elevated excitation power settings of $P_{exc} = 0.8$ and 1.2 µW, respectively. Using **Equation 3** to classify the emitters yields classification accuracies of 82.0% for the 0.8 µW datasets and 79.5% for the 1.2 µW datasets, both of which fall significantly below the high standard set by the results at 1 µW (i.e., 92.5% accuracy).[14,31] On the other hand, using LR to generate a new predictive model for QD and R6G at the two new powers yields higher default accuracies of 83.0% and 93.0% for 0.8 and 1.2 µW, respectively. The observations here further solidify the advantages of LR over metric-based analysis: it is substantially faster, more broadly applicable to various experimental conditions, and more accurate overall.

2.4 Conclusion

In this work, SMS is used to characterize the blinking of R6G and QD on a glass substrate for the purpose of distinguishing the emitters without measuring spectral color, a method called BBM. Blinking traces measure stochastic fluctuations in emissive intensity of single emitters over time, and these traces are analyzed by CPD, which parses out fourteen statistics that describe the behavior of the emitters. On average, the distributions of QD behavior falls above that of R6G for a number of

blinking statistics, including N_I and v_E, which can be attributed to their differences in photophysical blinking mechanism. However, significant overlap in these distributions prevents accurate emitter classification with only one blinking statistic. In response, we design metric-based analysis and eventually machine learning analysis for accurate classification of single QD and R6G emitters.

BBM may be carried out through an empirically derived metric designed by experimentalists for the QD/R6G system under specific experimental conditions (i.e., glass substrate, P_{exc} = 1 μW, and t_{bin} = 10 ms). **Equation 3** is derived from the five blinking statistics with the best distributional separation in order to exaggerate their differences. When used in conjunction with a secondary metric (i.e., blinking activity past 150 s), this BBM approach achieves accuracy of 92.5%. Furthermore, applying metric analysis to mixed QD and R6G samples of known composition yields excellent agreement between BBM prediction and expected values. These preliminary results demonstrate the promise of BBM as a novel SRI tool. However, specially crafting an empirical metric to the conditions of a particular experiment significantly limits the scope of its applications. M-based analysis distinguishes QD and R6G only under the given conditions of this experiment and cannot necessarily be applied to other emitters and other conditions. Consequently, machine learning is used as an alternative approach to BBM analysis.

Machine learning techniques like LR allow for rapid, automated classification of any system of emitters under any experimental conditions. LR creates an accurate (92.7%) model for classifying QD and R6G in less than a minute. Furthermore,

accuracy may be significantly improved by applying a classification threshold with high data retention (e.g., ~98% accuracy is achieved with ~75% data retention). Between its elevated accuracy, tunable classification threshold, rapid model generation, and generalizability to other systems, LR-based BBM is superior to the metric-oriented design.

These studies, especially the development of LR analysis, establish BBM as a powerful new tool for classifying emitters. Because of the adaptability of LR, these experiments also raise interesting questions regarding the performance of BBM with other fluorophore systems and experimental conditions. QD and R6G are very dissimilar emitters in structure, blinking mechanism, and fluorescence behavior, which made for an excellent proof-of-concept study. To expand the capabilities of BBM (e.g., a wider array of emitters for selection), LR performance must be tested on emitters that are more similar in nature, such as other organic fluorophores. Furthermore, experimental conditions such as labeling density and P_{exc} have the potential to effect, and even enhance, BBM accuracy. Investigating the impacts of these variables will allow us to tune and optimize BBM performance. Finally, studying more complex sample environments is a crucial step for broadening the applicability of BBM. The goal is to apply this novel approach to SRI experiments, which have much more environmental complexity than the glass substrate utilized in this study. In the next chapter, two of these considerations—imaging environment and emitter system—are investigated with the BBM methodology established here.

References

(1)   Cohen, S.; Valm, A. M.; Lippincott-Schwartz, J. Interacting Organelles. *Curr. Opin. Cell Biol.* **2018**, *53*, 84–91. https://doi.org/10.1016/j.ceb.2018.06.003.

(2)   Valm, A. M.; Cohen, S.; Legant, W. R.; Melunis, J.; Hershberg, U.; Wait, E.; Cohen, A. R.; Davidson, M. W.; Betzig, E.; Lippincott-Schwartz, J. Applying Systems-Level Spectral Imaging and Analysis to Reveal the Organelle Interactome. *Nature* **2017**, *546* (7656), 162–167. https://doi.org/10.1038/nature22369.

(3)   Möckl, L.; Moerner, W. E. Super-Resolution Microscopy with Single Molecules in Biology and Beyond–Essentials, Current Trends, and Future Challenges. *J. Am. Chem. Soc.* **2020**, *142* (42), 17828–17844. https://doi.org/10.1021/jacs.0c08178.

(4)   Abbe, E. Beiträge zur Theorie des Mikroskops und der mikroskopischen Wahrnehmung. *Arch. Für Mikrosk. Anat.* **1873**, *9* (1), 413–468. https://doi.org/10.1007/BF02956173.

(5)   Lerner, E.; Cordes, T.; Ingargiola, A.; Alhadid, Y.; Chung, S.; Michalet, X.; Weiss, S. Toward Dynamic Structural Biology: Two Decades of Single-Molecule Förster Resonance Energy Transfer. *Science* **2018**, *359* (6373), eaan1133. https://doi.org/10.1126/science.aan1133.

(6)   Yang, H.; Luo, G.; Karnchanaphanurach, P.; Louie, T.-M.; Rech, I.; Cova, S.; Xun, L.; Xie, X. S. Protein Conformational Dynamics Probed by Single-Molecule Electron Transfer. *Science* **2003**, *302* (5643), 262–266. https://doi.org/10.1126/science.1086911.

(7)   Ha, T.; Enderle, T.; Ogletree, D. F.; Chemla, D. S.; Selvin, P. R.; Weiss, S. Probing the Interaction between Two Single Molecules: Fluorescence Resonance Energy Transfer between a Single Donor and a Single Acceptor. *Proc. Natl. Acad. Sci.* **1996**, *93* (13), 6264–6268. https://doi.org/10.1073/pnas.93.13.6264.

(8)   Kopera, K. M.; Tuckman, H. G.; Hoy, G. R.; Wustholz, K. L. Origin of Kinetic Dispersion in Eosin-Sensitized TiO2: Insights from Single-Molecule Spectroscopy. *J. Phys. Chem. C* **2021**, *125* (43), 23634–23645. https://doi.org/10.1021/acs.jpcc.1c07597.

(9)   Kinkhabwala, A.; Yu, Z.; Fan, S.; Avlasevich, Y.; Müllen, K.; Moerner, W. E. Large Single-Molecule Fluorescence Enhancements Produced by a Bowtie Nanoantenna. *Nat. Photonics* **2009**, *3* (11), 654–657. https://doi.org/10.1038/nphoton.2009.187.

(10)   Rust, M. J.; Bates, M.; Zhuang, X. Sub-Diffraction-Limit Imaging by Stochastic Optical Reconstruction Microscopy (STORM). *Nat. Methods* **2006**, *3* (10), 793–796. https://doi.org/10.1038/nmeth929.

(11)   Huang, B.; Babcock, H.; Zhuang, X. Breaking the Diffraction Barrier: Super-Resolution Imaging of Cells. *Cell* **2010**, *143* (7), 1047–1058. https://doi.org/10.1016/j.cell.2010.12.002.

(12)   Lelek, M.; Gyparaki, M. T.; Beliu, G.; Schueder, F.; Griffié, J.; Manley, S.;
         Jungmann, R.; Sauer, M.; Lakadamyali, M.; Zimmer, C. Single-Molecule
         Localization Microscopy. *Nat. Rev. Methods Primer* **2021**, *1* (1), 1–27.
         https://doi.org/10.1038/s43586-021-00038-x.

(13)   Huang, T.; Phelps, C.; Wang, J.; Lin, L.-J.; Bittel, A.; Scott, Z.; Jacques, S.;
         Gibbs, S. L.; Gray, J. W.; Nan, X. Simultaneous Multicolor Single-Molecule
         Tracking with Single-Laser Excitation via Spectral Imaging. *Biophys. J.* **2018**,
         114 (2), 301–310. https://doi.org/10.1016/j.bpj.2017.11.013.

(14)   DeSalvo, G. A.; Hoy, G. R.; Kogan, I. M.; Li, J. Z.; Palmer, E. T.; Luz-Ricca,
         E.; de Gialluly, P. S.; Wustholz, K. L. Blinking-Based Multiplexing: A New
         Approach for Differentiating Spectrally Overlapped Emitters. *J. Phys. Chem.
         Lett.* **2022**, *13* (22), 5056–5060. https://doi.org/10.1021/acs.jpclett.2c01252.

(15)   Tan, J. A.; Rose, J. T.; Cassidy, J. P.; Rohatgi, S. K.; Wustholz, K. L.
         Dispersive Electron-Transfer Kinetics of Rhodamines on TiO2: Impact of
         Structure and Driving Force on Single-Molecule Photophysics. *J. Phys. Chem.
         C* **2016**, *120* (37), 20710–20720. https://doi.org/10.1021/acs.jpcc.6b01960.

(16)   Cordones, A. A.; Bixby, T. J.; Leone, S. R. Evidence for Multiple Trapping
         Mechanisms in Single CdSe/ZnS Quantum Dots from Fluorescence
         Intermittency Measurements over a Wide Range of Excitation Intensities. *J.
         Phys. Chem. C* **2011**, *115* (14), 6341–6349. https://doi.org/10.1021/jp2001223.

(17)   Wong, N. Z.; Ogata, A. F.; Wustholz, K. L. Dispersive Electron-Transfer
         Kinetics from Single Molecules on TiO2 Nanoparticle Films. *J. Phys. Chem. C*
         2013, *117* (41), 21075–21085. https://doi.org/10.1021/jp405899v.

(18)   Zondervan, R.; Kulzer, F.; Orlinskii, S. B.; Orrit, M. Photoblinking of
         Rhodamine 6G in Poly(Vinyl Alcohol): Radical Dark State Formed through
         the Triplet. *J. Phys. Chem. A* **2003**, *107* (35), 6770–6776.
         https://doi.org/10.1021/jp034723r.

(19)   Yeow, E. K. L.; Melnikov, S. M.; Bell, T. D. M.; De Schryver, F. C.; Hofkens,
         J. Characterizing the Fluorescence Intermittency and Photobleaching Kinetics
         of Dye Molecules Immobilized on a Glass Surface. *J. Phys. Chem. A* **2006**, *110*
         (5), 1726–1734. https://doi.org/10.1021/jp055496r.

(20)   Albery, W. J.; Bartlett, P. N.; Wilde, C. P.; Darwent, J. R. A General Model for
         Dispersed Kinetics in Heterogeneous Systems. *J. Am. Chem. Soc.* **1985**, *107*
         (7), 1854–1858. https://doi.org/10.1021/ja00293a008.

(21)   Tan, J. A.; Rose, J. T.; Cassidy, J. P.; Rohatgi, S. K.; Wustholz, K. L.
         Dispersive Electron-Transfer Kinetics of Rhodamines on TiO2: Impact of
         Structure and Driving Force on Single-Molecule Photophysics. *J. Phys. Chem.
         C* **2016**, *120* (37), 20710–20720. https://doi.org/10.1021/acs.jpcc.6b01960.

(22)   Cordones, A. A.; Leone, S. R. Mechanisms for Charge Trapping in Single
         Semiconductor Nanocrystals Probed by Fluorescence Blinking. *Chem. Soc.
         Rev.* **2013**, *42* (8), 3209. https://doi.org/10.1039/c2cs35452g.

(23)   Kuno, M.; Fromm, D. P.; Hamann, H. F.; Gallagher, A.; Nesbitt, D. J.
         Nonexponential "Blinking" Kinetics of Single CdSe Quantum Dots: A

Universal Power Law Behavior. *J. Chem. Phys.* **2000**, *112* (7), 3117–3120. https://doi.org/10.1063/1.480896.

(24) Reaser, B. C.; Wright, B. W.; Synovec, R. E. Using Receiver Operating Characteristic Curves To Optimize Discovery-Based Software with Comprehensive Two-Dimensional Gas Chromatography with Time-of-Flight Mass Spectrometry. *Anal. Chem.* **2017**, *89* (6), 3606–3612. https://doi.org/10.1021/acs.analchem.6b04991.

(25) Hajian-Tilaki, K. Receiver Operating Characteristic (ROC) Curve Analysis for Medical Diagnostic Test Evaluation. *Casp. J. Intern. Med.* **2013**, *4* (2), 627–635.

(26) Stoltzfus, J. C. Logistic Regression: A Brief Primer. *Acad. Emerg. Med.* **2011**, *18* (10), 1099–1104. https://doi.org/10.1111/j.1553-2712.2011.01185.x.

(27) Mater, A. C.; Coote, M. L. Deep Learning in Chemistry. *J. Chem. Inf. Model.* **2019**, *59* (6), 2545–2559. https://doi.org/10.1021/acs.jcim.9b00266.

(28) LeCun, Y.; Bengio, Y.; Hinton, G. Deep Learning. *Nature* **2015**, *521* (7553), 436–444. https://doi.org/10.1038/nature14539.

(29) Boni, Y. T.; Cammarota, R. C.; Liao, K.; Sigman, M. S.; Davies, H. M. L. Leveraging Regio- and Stereoselective C(Sp3)–H Functionalization of Silyl Ethers to Train a Logistic Regression Classification Model for Predicting Site-Selectivity Bias. *J. Am. Chem. Soc.* **2022**, *144* (34), 15549–15561. https://doi.org/10.1021/jacs.2c04383.

(30) Kirasich, K.; Smith, T.; Sadler, B. Random Forest vs Logistic Regression: Binary Classification for Heterogeneous Datasets. *SMU Data Sci. Rev.* **2018**, *1* (3).

(31) Hoy, G. R.; DeSalvo, G. A.; Haile, S. H.; Smith, E. N.; Wustholz, K. L. Rapid, Accurate Classification of Single Emitters in Various Conditions and Environments for Blinking-Based Multiplexing. *J. Phys. Chem. A* **2023**, *127* (15), 3518–3525. https://doi.org/10.1021/acs.jpca.3c00917.

Chapter III: Blinking-Based Multiplexing in Model Biological Environments

3.1 Introduction

Fluorescence imaging of nanoscale biological systems is critical to understanding their structures, functions, and inter/intracellular interactions.[1,2] Multicolor super-resolution imaging (SRI) allows for such systems to be visualized with unprecedented spatial resolution.[3–5] However, because multicolor SRI relies on spectral color for emitter identification, there are few sets of emitters that can be used together due to incompatible experimental conditions and limited availability of high-performance probes across the visible spectrum. Even relatively small overlaps in emission spectra can lead to inaccuracy called spectral crosstalk. To overcome this challenge, many researchers turn to sequential imaging of emitters, which eliminates the effects of crosstalk but also increases experimental time and demands.[6,7]

Blinking-based multiplexing (BBM) is a novel multicolor imaging tool that eliminates the reliance on spectral color for emitter identification by instead exploiting their intrinsic blinking dynamics.[8] Blinking, defined as random fluctuations of single emitters under continuous photoexcitation, is a natural phenomenon that is observed only at the single-molecule level. The blinking dynamics of single emitters are highly dependent not only on their chemical identity but also the conditions of the local environment. That is, single molecules of the same class display dispersive behavior depending on factors such as molecular orientation or proximity to other molecules.[9] The initial BBM experiment separating quantum dots (QD) from rhodamine 6G (R6G) emitters demonstrated a successful proof-of-concept, but also generated questions

about BBM's performance under various experimental conditions. Although BBM was initially performed using an empirically-derived metric, this approach is time-intensive and limits the scope of BBM. Logistic regression (LR), a machine learning technique, offers a much faster, more generalizable approach by generating predictive models for QD and R6G under various experimental conditions. For instance, classification accuracies of 95% are routinely achieved for QD and R6G on glass with various excitation powers (P_{exc}) and bin times (t_{bin}) using LR and classification thresholding.[10] In each experiment, LR successfully adapts to the unique blinking distributions of each system to rapidly generate high-performance models for emitter classification.

There are several additional variables to investigate to both optimize and broaden the applicability of BBM for biological imaging. BBM control experiments were performed on a simple glass environment, making substrate a crucial variable for investigation before BBM can be applied to more complex systems (e.g., biological structures). Additionally, it is necessary to expand the capabilities of BBM to differentiate more than two spectrally-overlapped probes, as otherwise it will face the same limitations as current multicolor imaging techniques. Organic dyes are of particular interest due to their small size and greater biocompatibility as compared to inorganic nanoparticles. In this chapter, the environmental and molecular dependence of BBM are investigated using the polymer poly(vinyl alcohol) (PVA) as a model biological environment for emitter immobilization and a boron-dipyrromethene (BODIPY) dye as a new probe for the BBM library.

3.1.1 Poly(vinyl Alcohol) as a Model Biological Environment

First, BBM of the previously established QD and R6G system is tested in a new, more complex environment. Because single-molecule blinking behavior is closely related to local environment, altering substrate is likely to impact an emitter's blinking mechanism (e.g., by allowing access to new dark states or offering greater photostability). Ultimately, BBM is meant to be utilized in biological imaging experiments, which involve a much higher degree of environmental complexity than the simple glass substrates used in Chapter 2. It is therefore reasonable to suspect qualitative and quantitative changes in the blinking of QD and R6G in such an environment. To establish the viability of BBM for complex imaging applications, we test its performance with a model biological environment: poly(vinyl alcohol) (PVA).

Figure 1. Structure of poly(vinyl alcohol).

PVA is a linear polymer with an alternating hydroxyl unit (**Figure 1**), synthesized from the full or partial hydrolysis of poly(vinyl acetate).[11,12] The properties of PVA, including glass transition temperature (T_g), crystallinity, and viscosity, are highly dependent on its degree of hydrolysis and molecular weight (MW). Experiments in this chapter use 88% hydrolyzed PVA with MW ~15 kDa, which, according to the manufacturer, has a viscosity of 4.1 cPs for a 4% aqueous solution. T_g, the temperature at which PVA transitions from a rigid to a flexible state, has been reported to range from ~70-90 °C, with higher values corresponding to higher degrees of hydrolysis and lower values indicating higher water content.[11,13,14] Above this temperature, PVA

becomes mobile and flexible, which has been shown to affect the photophysics of embedded fluorophores.[13,15–17] At room temperature, however, the rigidity of PVA immobilizes emitters and offers greater structural stability.[18]

PVA is known to introduce alternative blinking pathways that alter the fluorescent behavior of embedded emitters. For R6G in particular, the hydroxyl groups of PVA are thought to donate an electron to the lowest triplet state (T_1) of R6G, producing a radical anion of R6G and forcing it into a reversible dark state.[19] This electron transfer process is dependent on intermolecular distance between the dye and a PVA hydroxyl site, which leads to a broad distribution of the lifetimes of fluorescent events, which can be probed with SMS. For QD in PVA, it has been proposed that dark states arise due to the stabilization of charges ejected from the emitter to self-trapped states in the polymer matrix.[20]

PVA has already been used as a model biological environment in numerous single-molecule studies.[14,19,21–23] Bittel et al. has demonstrated effective use of emitter immobilization in PVA as a simple yet effective method for screening fluorophores for potential use in SRI.[21] The study and characterization of photophysical properties commonly involves fluorophore immobilization via labeling a known cell structure or protein conjugation to glass. However, fluorophores embedded in PVA and conjugated to glass displayed similar photophysical behavior, indicating that PVA is a faster, simpler alternative for evaluating emitters. Furthermore, PVA also has a myriad of favorable characteristics that make it attractive for biological studies. As a biocompatible polymer, PVA is nontoxic to living cells and has extensive applications

in the biomedical field, including drug delivery and wound care, as well as food science.[24–27] Furthermore, below T_g, PVA creates a more rigid, less reactive environment for probes than simple aqueous solution, which offers greater structural stability for fluorophores.[14,18] Between its simplicity for experimental use, its biocompatibility, and its composition of polar and nonpolar groups, PVA serves as a model system that mimics a biological setting.

3.1.2 Properties of Pyrromethene 605

In addition to studying BBM environment, this chapter expands the library of BBM emitters by investigating the behavior of an organic BODIPY fluorophore, both on glass and in PVA. BODIPY dyes are becoming increasingly popular in imaging experiments due to their small size, spectral stability, narrow emission bandwidth, and compatibility with live cells.[22,28–32] These dyes demonstrate significant spectral tunability over the visible region with only slight structural variations.[33–35] Additionally, BODIPY derivatives can be synthetically engineered to have a wide range of Stokes shifts, which has allowed for successful simultaneous imaging of two or more probes via spectral discrimination.[22,31] However, such a library of tunable emitters is not commercially available, and the design and
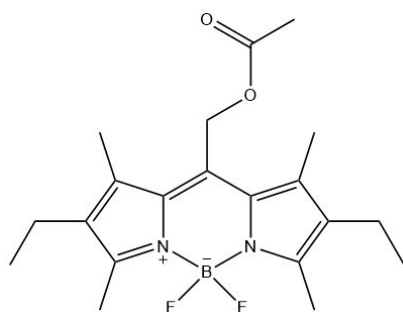
Figure 2. Structure of PM605.

synthesis of each probe is time-intensive and so far unavailable to SRI practitioners. Furthermore, despite widespread interest in BODIPY dyes due to their favorable

emissive properties, the blinking mechanism of this family of molecules is poorly understood.

Pyrromethene 605 (PM605), is a commercially-available BODIPY derivative (**Figure 2**). According to the manufacturer, PM605 has a quantum yield of 0.74 and an extinction coefficient of 7.76×10^4 M^{-1} cm^{-1} at its maximum absorption wavelength of 543 nm. The high extinction coefficient and quantum yield, along with significant spectral overlap with QD and R6G (**Figure 3**) make PM605 a good candidate for BBM at 532 nm laser excitation. In this chapter, the blinking dynamics of PM605 on glass and in PVA are examined to investigate its blinking mechanism and establish it as a viable BBM probe.
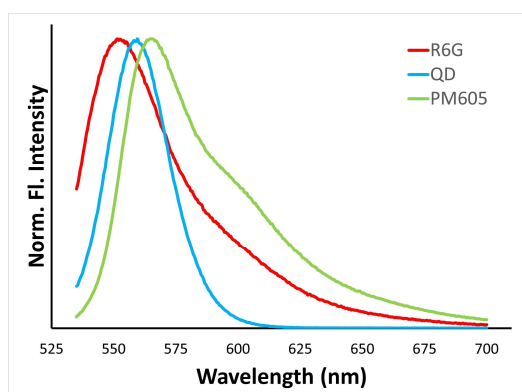
Figure 3. Emission spectra of R6G, QD, and PM605 display significant overlap.

3.2 Methods

3.2.1 Materials and Sample Preparation

R6G (Acros Organics, 99%) and PM605 (Exciton) were used as received. All glassware was cleaned in a base bath (~1 M KOH) for 12-24 h and rinsed with ultrapure water (ThermoScientific, EasyPure II, 18.2 MΩ cm). Microscope coverslips (Fisher Scientific, 12-545-102) were base bathed for 12-24 h, rinsed with ultrapure water, and dried with clean air (Wilkerson, X06-02-000). R6G stock solutions (~10^{-4} M) were

prepared in ultrapure water, and PM605 stock solutions ($\sim 10^{-4}$ M) were prepared in ethanol (Pharmco, absolute anhydrous, 200 proof). QD stock solutions (Invitrogen, Qdot 565 ITK carboxyl quantum dots, 8 µM solution in borate buffer) were used as received. Stock solutions of R6G and PM605 were sonicated for ~1 min before use. For QD and R6G experiments, solutions of 10% wt PVA were prepared by gradually adding powdered PVA (MP Biomedicals, 88% hydrolyzed, MW ~15 kDa) to ultrapure water heated to 40 ℃. For use in PM605 experiments, solutions of 10% wt PVA were prepared by gradually adding powdered PVA to a 1:1 v/v mixture of ultrapure water to EtOH heated to 40 ℃. For thorough mixing, the solutions were gently stirred at 65 ℃ for several hours before being transferred to a rotator (Fisher Scientific, Multi-Purpose Tube Rotator, 88861049) for 12-24 h at 5 rpm.

For PM605 experiments on glass, an ethanolic stock solution was diluted to 1 nM to achieve appropriate labeling density for single-molecule studies. Samples were prepared by spin coating 35 µL of the resulting PM605 solution onto a clean glass coverslip using a spin coater (Laurell Technologies, WS-400-6NPP-LITE) operating at 3000 rpm with a 5 s acceleration time and a 30 s spin time. Consistent with previous single-molecule studies in PVA, emitter solutions were prepared in 10% wt PVA solutions.[13,36] QD and R6G were diluted to final concentrations of 4 nM and 10 nM, respectively, in aqueous PVA solution. PM605 was diluted to a final concentration of 2 nM in 1:1 EtOH to ultrapure water PVA solution. The resulting R6G/PVA, QD/PVA, and PM605/PVA solutions were mixed on a rotator for 12-24 h at 5 rpm. To achieve a thin polymer film (i.e., ~250 nm thickness) with evenly dispersed emitters, single-

molecule samples were prepared by spin coating 100 μL of one of the three aforementioned emitter/PVA solutions onto a coverslip at 3000 rpm with a 5 s acceleration time and 30 s spin time.[13] To reduce the amount of adsorbed water in the emitter/PVA samples, which has been found to reduce the emission intensity of fluorophores via vibrational relaxation, the prepped slides were stored under vacuum overnight before use.[23]

3.2.2 Single-Molecule Spectroscopy and Data Analysis

Single-molecule samples were mounted onto a custom aluminum flow cell (approximately $1.5" \times 3" \times 0.5"$ and equipped with Tygon tubing) and flushed with dry nitrogen gas (Airgas, 100%). The flow cell was placed on a nanopositioning stage (Physik Instrumente, LP E-545) atop an inverted confocal microscope (Nikon, TiU). Using a high numerical aperture (NA) 100x oil-immersion objective (Nikon Plan Fluor, NA = 1.3), laser excitation at 532 nm (Spectra Physics, Excelsior) was focused to a diffraction limited spot. Excitation powers (P_{exc}) of 0.8 and 1 μW were used for PM605/glass and emitter/PVA experiments, respectively, to maximize emission signal while limiting molecular photobleaching. Sample emission was collected through the objective and passed through an edge filter (Semrock, LP03-532RS-2S) before being focused to an avalanche photodiode detector (APD) with a 50 μm aperture (MPD, PDM050CTB) to achieve confocal resolution. Focus during raster scans was maintained using a z-axis microscope lock (Applied Science Instruments, MFC-2000). A custom LabView program was used to control the nanopositioning stage and collect

the corresponding emission intensities, which were measured with a 30 ms dwell time. Single emitters were identified on the observations of blinking dynamics, diffraction-limited spots, irreversible molecular photobleaching, and/or concentration dependence of spot density. All blinking traces were collected over 200 s with t_{bin} = 10 ms.

Blinking traces were analyzed using the change point detection (CPD) method described in Chapter 2, which determines the statistically significant intensities of each trace and their corresponding temporal durations to quantify the blinking dynamics of each emitter. Ten independent CPD blinking statistics are used in LR for generating models. Four statistics describe the intensity levels of a trace: the number of unique intensity levels (N_I), minimum emissive intensity (I_{min}), maximum emissive intensity (I_{max}), and average intensity level over the entire trace duration ($\langle I \rangle_t$). I_{min} is defined as one standard deviation above the minimum deconvolved intensity level. LR also includes several statistics that describe the number and durations of emissive and nonemissive segments and intervals: number of on segments ($N_{on,seg}$), number of off segments ($N_{off,seg}$), average on-segment time ($\langle t_{on,seg} \rangle$), average off-segment time ($\langle t_{off,seg} \rangle$), average on-interval time ($\langle t_{on,int} \rangle$), and average-off interval time ($\langle t_{off,int} \rangle$). Segments are events at one intensity level, and intervals include all successive segments that occur before a switch between on and off. By fitting the statistics of each emitter system to a 10-dimensional sigmoid function (i.e., one dimension per included CPD statistic), LR generates a model that gives the classification probability of a single emitter (P_A) as a function of input predictors. A more detailed description of LR is found in Chapter 2.

3.3 Results and Discussion

3.3.1 Blinking Dynamics of QD and R6G in PVA

To test the performance of BBM in the more biologically relevant PVA environment, blinking dynamics of hundreds of QD and R6G emitters in PVA are collected at 532 nm excitation and $P_{exc} = 1$ μW. Typically, in single-molecule experiments, the presence of single emitters is determined by the appearance of bright diffraction-limited spots with significant contrast from a dim background. However, **Figure 4A**, which shows a typical false-colored emission scan of 10 nM R6G/PVA, displays increased background signal that is not observed for corresponding measurements of emitters on glass. To determine if the elevated background signal is
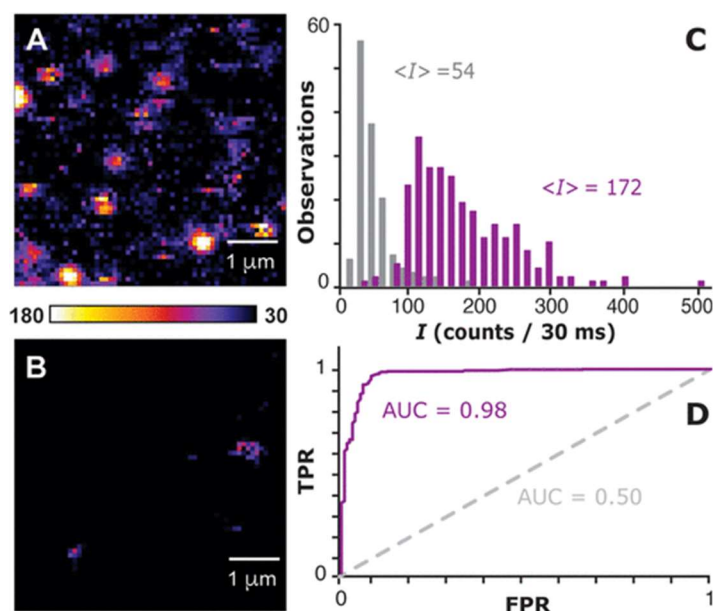
Figure 4. (A) Representative emission scan of 10 nM R6G in PVA at $P_{exc} = 1$ μW. (B) Emission images of blank 10% wt PVA under the same conditions display dim diffraction-limited spots and high intensity pixels across the scans due to polymer impurities and/or scattering from aggregates. (C) Histograms of I values for 138 blank PVA spots (gray) and 261 R6G and QD emitters in PVA (purple) are well separated. (D) ROC curve analysis of the I threshold (purple) as compared to the hypothetical case when a classifier cannot distinguish (gray). A high AUC establishes I as an effective parameter for distinguishing true emitters from PVA background signal.

due to the polymer film, blank PVA samples were prepared using the same methods but without the addition of emitters. 30 emission images of blank PVA were measured (**Figure 4B**) and compared to corresponding images of emitter samples. These scans display dim diffraction-limited spots and high-intensity pixels scattered throughout the scan. The source of these features is thought to be due to impurities and/or scattering from large aggregates of PVA. To ensure that background signal from PVA is excluded from true emitter datasets, the distribution of emission image intensities (I) is found by sampling values for 138 blank PVA, 124 R6G/PVA, and 137 QD/PVA spots (**Figure 4C**). The latter two are grouped together as "emitter/PVA" for analysis purposes. The average emission intensity, $\langle I \rangle$, for blank PVA is 54 ± 2 counts per 30 ms, which falls significantly below the emitter/PVA average of 172 ± 4 counts per 30 ms. Furthermore, the overall I distributions for blank PVA and emitter/PVA are well separated.

Because of the excellent separation of the distributions, an I-based threshold is applied to ensure that blank PVA is excluded from the datasets of true QD and R6G emitters. Receiver operating characteristic (ROC) curve analysis (described in Chapter 2 in greater detail) is used to assess whether I is an appropriate criterion for identifying true emitters. The correct identification of QD or R6G as an emitter is defined as a true positive, and a false positive refers to the case where PVA background signal is incorrectly attributed to an emitter. Area under the curve (AUC) for the ROC curve, is 0.98 (**Figure 4D**). The closer an AUC value is to 1, the more effective the test parameter is for differentiation, so the high value here assures that I is an appropriate metric for
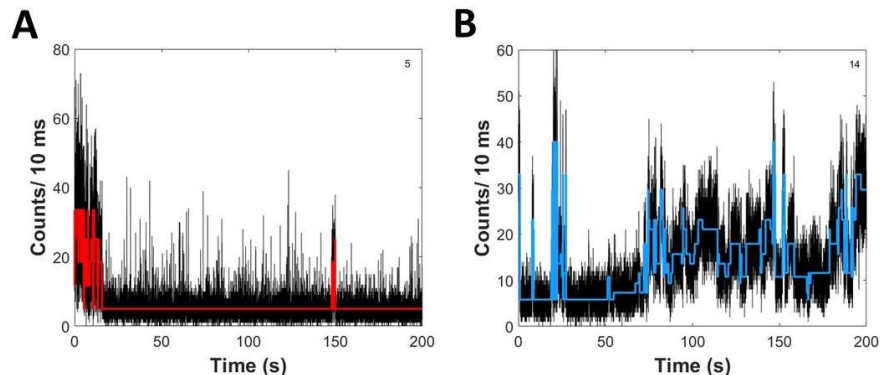
Figure 5. Representative blinking traces of (A) R6G/PVA and (B) QD/PVA at $P_{exc} = 1$ μW.

identifying true emitters. Next, the graph is examined to establish an appropriate threshold to maximize true positive rate (TPR) and minimize false positive rate (FPR). Another factor to consider in selecting a threshold is that it should not be set too high as to exclude excessive quantities of dim true emitter data. Considering these three elements, an I threshold value of 100 counts per 30 ms is selected, where $I \geq 100$ corresponds to an emitter and $I < 100$ to PVA background signal. Within this framework, a high TPR of 0.92 and low FPR of 0.06 are achieved, and just 20/261 (<8%) of diffraction-limited spots from the collective emitter/PVA dataset are attributed to PVA and need to be discarded. The threshold ensures that only true emitters are included in BBM analysis and comes at a low data loss rate. For the remainder of this work, we focus on the remaining 129 QD/PVA and 112 R6G/PVA spots and corresponding blinking traces (**Figure 5**) that are determined to be true emitters after applying the $I \geq 100$ counts per 30 ms threshold.

The blinking dynamics of QD and R6G emitters undergo significant changes in PVA as compared to glass (**Table 1**), consistent with previous studies.[8,19,37,38] Notably,

Blinking Statistic	QD		R6G	
	Glass	PVA	Glass	PVA
N_I	17.1 ± 0.6	12.4 ± 0.4	6.1 ± 0.3	6.5 ± 0.3
$N_{on,seg}$	270 ± 20	78 ± 5	29 ± 5	31 ± 5
$N_{off,seg}$	17 ± 1	14.2 ± 0.8	6.6 ± 0.8	10 ± 1
I_{min}	15 ± 2	8.6 ± 0.5	4.0 ± 0.2	6.6 ± 0.8
I_{max}	140 ± 10	43 ± 2	36 ± 4	24 ± 2
$\langle I \rangle_t$	54 ± 5	19 ± 1	4.7 ± 0.5	6.7 ± 0.4
$\langle t_{on,seg} \rangle$	1.2 ± 0.1	3.0 ± 0.3	2.3 ± 0.7	3.5 ± 0.5
$\langle t_{off,seg} \rangle$	2.2 ± 0.3	4.6 ± 0.5	15 ± 1	5.0 ± 0.4
$\langle t_{on,int} \rangle$	14 ± 1	15 ± 1	6 ± 1	10 ± 1
$\langle t_{off,int} \rangle$	3.1 ± 0.7	5.0 ± 0.4	11 ± 2	11 ± 2

Table 1. Average blinking statistics of R6G and QD emitters at $P_{exc} = 1$ µW on glass and in PVA for the 10 blinking statistics included in LR analysis. Errors correspond to standard deviations of the mean. Intensities are reported in counts/ 10 ms, and times are reported in seconds.

the emissive intensity of both emitters is decreased from glass to PVA. I_{max} decreases from 140 ± 10 to 43 ± 2 counts per 10 ms and 36 ± 4 to 24 ± 2 counts per 10 ms for QD and R6G, respectively, which may be attributed to fluorescence quenching from PVA hydroxyl groups and adsorbed water reducing the emissive intensity of emitters via vibrational relaxation.[23,39] For the same reason, $\langle I \rangle_t$ decreases for QD/PVA as compared to glass. However, an increase in $\langle I \rangle_t$ is observed for R6G/PVA. Although this may appear contradictory to the decrease in I_{max}, it is important to note that R6G displays an increase in $\langle t_{on,int} \rangle$ when embedded in PVA. This observation, consistent with reports that polymer matrix may stabilize emitters, indicates that longer emissive events in PVA elevate $\langle I \rangle_t$ despite the diminished intensities.[18,40]

Average blinking statistics, however, do not tell the whole story. Although statistics such as $\langle t_{on,int} \rangle$ and $\langle t_{off,int} \rangle$ show little to no change between the glass and PVA environments, their distributions reveal shifts that are hidden by ensemble averaging. Complementary cumulative distribution functions (CCDFs)
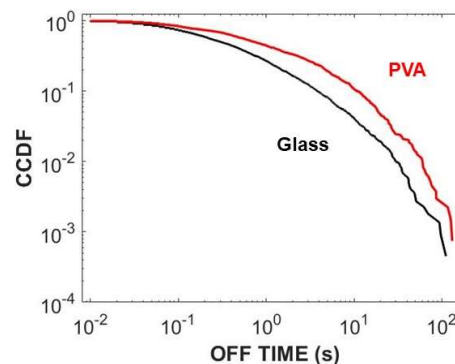
Figure 6. Off times CCDF for QD on glass (black) and in PVA (red) reveal differences in emitter blinking dynamics between the environments.

describe the probability of a blinking event lasting as long as or longer than a specified time; the distributions start at high probability for short blinking events and decrease as event duration increases. Qualitative assessment of CCDFs for QD and R6G on- and off-interval times corroborates the changes in blinking (**Appendix I, Figures A1-A2 and Tables A1-A2**). For instance, off-interval times for QD demonstrate modest broadening in PVA as compared to glass (**Figure 6**), consistent with previous observations of complex electron transfer (ET) in PVA.[14,19,38] All single-molecule experiments were performed well below T_g, so the altered blinking kinetics are attributed to the new blinking mechanisms in PVA rather than emitter rotation or photoinduced intramolecular rearrangement.[19] These changes confirm the dependence of single emitter blinking dynamics on local environment and establish PVA as a suitable model environment for BBM.

3.3.2 Blinking-Based Multiplexing of QD and R6G in PVA

To test the performance of BBM analysis in PVA, multinomial LR is performed on 129 QD/PVA and 112 R6G/PVA emitters. LR outputs the following best fit model in the form $P_{QD} = [1 + e^{-z}]^{-1}$, where

$$z = 2.8\langle I\rangle_t + 2.7N_I - 1.9N_{on,seg} - 0.7\langle t_{off,seg}\rangle + 0.6I_{min} + 0.4N_{off,seg} -$$

$$0.2I_{max} + 0.2\langle t_{on,seg}\rangle - 0.2\langle t_{on,int}\rangle - 0.2\langle t_{off,int}\rangle + 1.1 \tag{1}$$

with regression coefficients listed in descending magnitude. The magnitude of a coefficient indicates the model's sensitivity to the corresponding blinking statistic for classifying emitters. That is, blinking statistics that have well-separated distributions result in larger coefficients and therefore are more influential in LR predictions. In this framework, $\langle I\rangle_t$, N_I, and $N_{on,seg}$ are the most important statistics for distinguishing R6G and QD in PVA, whereas average interval and on-segment times (i.e., $\langle t_{on,int}\rangle$, $\langle t_{off,int}\rangle$, and $\langle t_{on,seg}\rangle$) play relatively modest roles in classification.
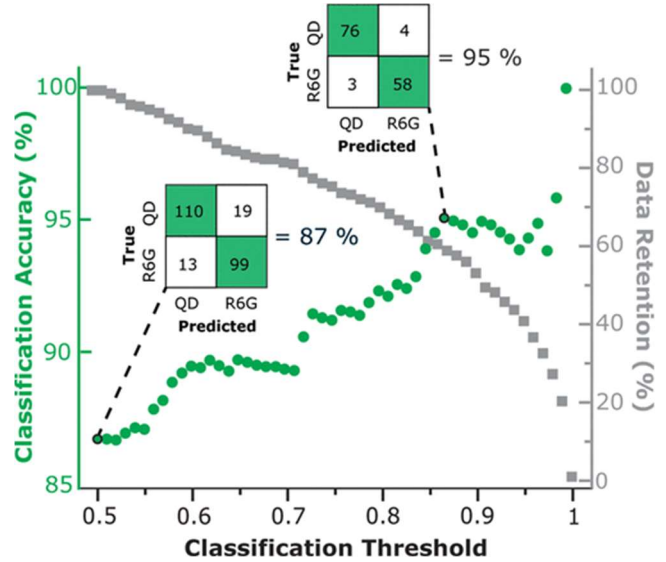
Figure 7. Classification accuracy (green) and data retention (gray) for BBM of QD and R6G in PVA at $P_{exc} = 1$ μW via multinomial LR as classification threshold is varied. Inset confusion matrices reveal LR performance at the default binary classification threshold and a threshold of 0.87. The default yields 87% accuracy and retains 100% of the data, whereas at the 0.87 threshold, accuracy reaches 95% but ~40% of data points are discarded.

Using the default classification threshold for a binomial system (i.e., P_{QD} or $P_{R6G} > 0.5$ results in classification as QD or R6G, respectively), LR yields an accuracy of 86.7% with TPR = 0.85 and FPR = 0.12. Although LR performs well here, it does not reach the standard set by previous experiments of QD and R6G on glass (92.7% default accuracy). However, as described in Chapter 2, applying a classification threshold increases accuracy and TPR and decreases FPR by discarding less certain data points. **Figure 7** shows the balance between overall classification accuracy and data retention as the threshold is increased from the default. At a threshold of 0.87, BBM via LR reaches accuracy as high as 95% for this system with TPR = 0.95 and FPR = 0.05, but it does so with only ~60% data retention. However, in data-dense experiments such as single-molecule localization microscopy (SMLM), data loss is a fair trade for high accuracy.

In addition to testing the ability of LR to classify emitters, we also investigate its ability to distinguish between environments. That is, two multinomial LR classifications are performed to compare emitters on glass versus in PVA. **Table 2** summarizes the resulting coefficients from both analyses. For R6G, LR classifies glass and PVA environments with a default accuracy of 88.1%, TPR = 0.91, and FPR = 0.18. For QD, LR is less successful at distinguishing local environment, yielding default accuracy of 76.1%, TPR = 0.71, and FPR = 0.18. Varying the classification threshold once again improves BBM performance. Environmental classification of R6G reaches 95% accuracy, TPR = 0.98, and FPR = 0.08 with 64.2% data retention when a classification threshold of 0.91 is applied. That level of accuracy can be matched for

LR coefficient	Emitter	Environment	
	QD vs R6G in PVA	R6G on glass vs PVA	QD on glass vs PVA
N_I	2.7	-1.3	-1.2
$N_{on,seg}$	-1.9	-0.7	3.0
$N_{off,seg}$	0.4	0.4	~0
I_{min}	0.6	-4.8	1.7
I_{max}	-0.2	4.1	1.7
$\langle I \rangle_t$	2.8	0.7	-0.7
$\langle t_{on,seg} \rangle$	0.2	0.1	0.3
$\langle t_{off,seg} \rangle$	-0.7	0.3	-0.6
$\langle t_{on,int} \rangle$	-0.2	-0.8	0.2
$\langle t_{off,int} \rangle$	-0.2	0.4	0.6
b	1.1	0.7	0.8

Table 2. LR coefficients for emitter and environmental classifications at $P_{exc} = 1$ μW. Best fit parameters correspond to each of the 10 blinking statistic included in LR as well as an intercept (b).

QD as well but comes at a much more substantial cost with data retention as low as 29.0%. Nonetheless, the results here suggest that environmental classification via LR is promising. Such a technique would be valuable for imaging multicomponent systems, where LR can be used to simultaneously predict both emitter class and environment.

3.3.3 Blinking Dynamics of PM605 on Glass and in PVA

To investigate if BBM is successful with emitters beyond just QD and R6G, blinking dynamics of 118 PM605 molecules on glass and 109 PM605 molecules in PVA were collected at $P_{exc} = 0.8$ and 1 μW, respectively. Similar to the QD and R6G experiments described in previous sections, PVA is observed to add complexity to emitter identification and analysis. However, unlike QD/PVA and R6G/PVA,
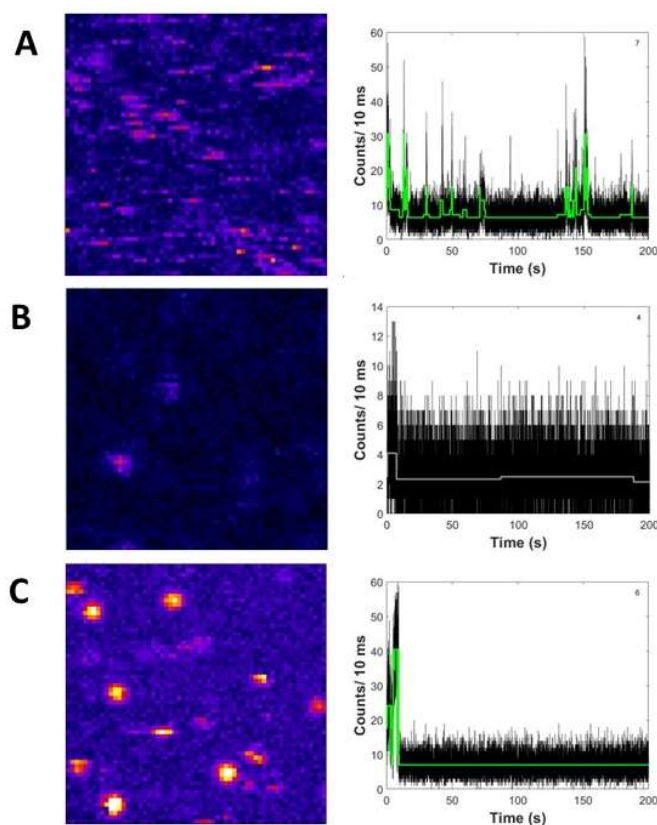
Figure 8. Representative emission scans (left) and blinking dynamics (right) of (A) PM605/PVA at P_{exc} = 1 μW, (B) blank mixed solvent PVA at P_{exc} = 1 μW, and (C) PM605/glass at P_{exc} = 0.8 μW. All emission images are presented on a scale of 0-250 counts/ 30 ms.

PM605/PVA emission scans have dimmer intensities on average and lack diffraction-limited spots (**Figure 8A**). Therefore, identifying the presence of single molecules is more difficult in this system, and an *I*-based threshold is no longer suitable for separating true molecules from background polymer scattering. To distinguish PM605 emitters from background PVA, blinking dynamics of PM605/PVA are compared to that of blank 10% wt PVA made in 1:1 EtOH to ultrapure water. Despite the presence of some low intensity diffraction-limited spots in emission images (**Figure 8B**), likely due to scattering from polymer aggregates or fluorescent impurities, blank PVA demonstrates little to no fluorescence or blinking behavior on average. The average emission image intensity, $\langle I \rangle$, of 56 ± 6 counts/ 30 ms for the 34 sampled blank PVA spots falls far below the average of 104 ± 3 counts/30 ms for PM605/PVA. These observations suggest that mistaking polymer background signal for a true PM605 emitter is not a significant issue in this system.

64

LR Coefficient	PM605 vs blank PVA	PM605 vs R6G in PVA	PM605 vs QD in PVA
N_I	69.5	2.0	18.2
$N_{on,seg}$	2.4	0.1	9.9
$N_{off,seg}$	0.4	1.4	2.5
I_{min}	119.7	5.7	29.1
I_{max}	21.0	-0.9	-6.6
$\langle I \rangle_t$	-141.9	-8.1	-125.5
$\langle t_{on,seg} \rangle$	1.6	-3.5	-12.4
$\langle t_{off,seg} \rangle$	-8.2	-1.2	1.1
$\langle t_{on,int} \rangle$	-1.6	0.4	-8.6
$\langle t_{off,int} \rangle$	6.6	0.4	8.3
b	31.8	-2.1	-52.2

Table 3. LR coefficients for identification of PM605 emitters in PVA and classification of PM605 against R6G and QD.

To confirm that blank PVA can be easily distinguished from emitters, LR is performed using blinking dynamics from 109 PM605/PVA and 34 blank PVA spots. The resulting coefficients are summarized in **Table 3**. Compared to other BBM experiments with LR (**Tables 2-3**), the coefficients here are substantially larger in magnitude, indicating a particularly high degree of separation in the distributions of blinking statistics. When the LR model is applied, the classification accuracy is 94.4%, as calculated from the confusion matrix shown in **Figure 9**. The high accuracy and large coefficients indicate that, in addition to being visually distinguishable, the blinking dynamics of blank PVA are quantifiably distinct from PM605/PVA. Because only a small fraction (3.5%) of blank PVA traces is predicted to be PM605 emitters, the contributions from background PVA are modest, and, accordingly, none of the 109 emitters are discarded from the PM605/PVA dataset.

Figure 9. LR confusion matrix for PM605/PVA vs. blank PVA yields classification accuracy of 94.4%, indicating that PM605 is easily distinguishable from PVA background.

Blinking Statistic	PM605/ Glass	PM605/ PVA
N_I	4.8 ± 0.3	8.1 ± 0.2
$N_{on,seg}$	12 ± 3	52 ± 4
$N_{off,seg}$	2.7 ± 0.4	30 ± 1
$N_{on,int}$	1.8 ± 0.4	19 ± 1
$N_{off,int}$	1.6 ± 0.4	19 ± 1
$\langle t_{on,seg} \rangle$	2.7 ± 0.4	0.60 ± 0.03
$\langle t_{off,seg} \rangle$	28 ± 3	6.8 ± 0.4
$\langle t_{on,int} \rangle$	8 ± 1	1.6 ± 0.1
$\langle t_{off,int} \rangle$	6 ± 2	11 ± 1

Table 4. Average blinking statistics of PM605 molecules at $P_{exc} = 0.8$ μW on glass and $P_{exc} = 1$ μW in PVA, respectively. Errors correspond to standard deviations of the mean. Values for $\langle t \rangle$ are reported in seconds.

Figures 8A and C show representative emission scans and blinking traces for PM605 on glass and in PVA, respectively. Qualitatively, dramatic differences are seen in the emission images of PM605 in the two environments. On glass, the fluorophores appear as round diffraction limited spots with high intensity. In polymer matrix, PM605 molecules are striped in appearance and display lower counts on average. In the blinking traces, PM605/glass emitters are initially bright but appear to quickly undergo irreversible photobleaching, whereas PM605/PVA blinks intermittently throughout the entire 200 s trace. The improved photostability in PVA is likely due to greater emitter stability in the polymer matrix.[40] These qualitative observations manifest in the average CPD statistics (**Table 4**). Most notably, PM605/PVA displays much shorter $\langle t_{on,seg} \rangle$ and $\langle t_{on,int} \rangle$ and greater $N_{on,seg}$, $N_{off,seg}$, $N_{on,int}$, and $N_{off,int}$ than on glass. Additionally, significant changes in $\langle t_{on/off,seg/int} \rangle$ are

observed in the CCDFs and associated fit parameters of the two datasets (**Appendix I, Figure A3 and Tables A3-A4**). Because the PM605 datasets on glass and in PVA were collected at slightly different P_{exc}, blinking statistics relating to emissive intensity values (i.e., I_{min}, I_{max}, and $\langle I \rangle_t$) are not compared.

To explain the changes in the single-molecule fluorescence behavior of PM605 in PVA as compared to glass, the underlying mechanism for blinking is examined. **Figure 10** shows CCDF plots of the on- and off-interval times for PM605/glass and PM605/PVA with lognormal fits overlaid. Most of the on- and off-interval times on glass and in PVA are appropriately modeled by lognormal distributions as indicated by nonzero p-values, which are statistical measures that describe goodness of fit. The p-value for PM605/PVA off-interval times is zero, which indicates a poor fit to a lognormal function despite visual agreement between the fit and the true distribution. However, **Table A3** in **Appendix I** reveals that the plot is not well modeled by a Weibull distribution (i.e., $p = 0$) and that a power law captures only a small portion of the distribution, as indicated
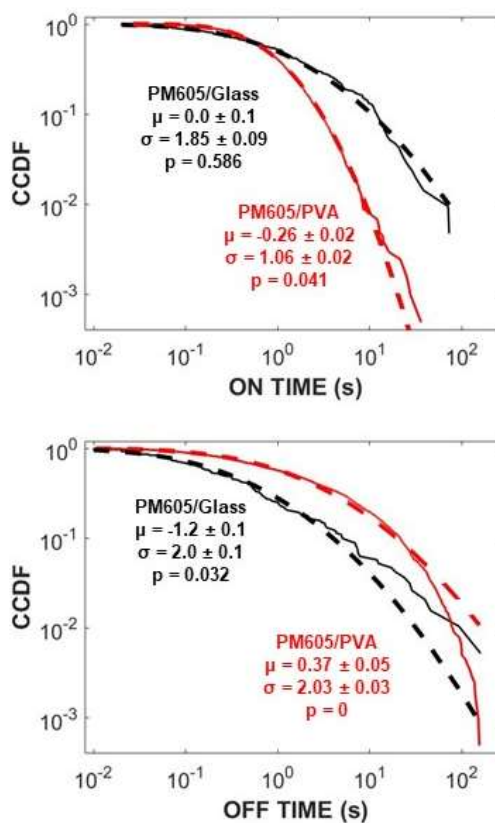
Figure 10. (A) On- and (B) off-interval time CCDFs for PM605 on glass (black) and in PVA (red). Lognormal fits to the data are presented as dashed overlays.

by a high onset time (t_{min} = 41.57 s). Therefore, despite its p-value of zero, a lognormal distribution is the most representative model of PM605/PVA off-interval times.

Lognormal distributions of on and off events are consistent with the Albery model for dispersive ET, which assumes Gaussian-distributed barriers to electron transfer.[37,41–43] The lognormally distributed on- and off-interval times for PM605 on glass and in PVA indicate that ET is the mechanism behind blinking in PM605 in both environments. According to the Albery model, $-\mu$ is proportional to the rate of ET (i.e., $-\mu_{on}$ and $-\mu_{off}$ indicate relative forward and back ET rates, respectively) and σ describes the degree of kinetic dispersion about μ. In this framework, a larger $-\mu_{on}$ value of 0.26 ± 0.02 in PVA as compared to 0.0 ± 0.1 on glass suggests that PM605 undergoes faster forward ET in PVA. PVA is known to be a heterogeneous environment, so we expect to observe greater dispersion on that substrate than on glass. Interestingly, dispersion is smaller in PVA for on-interval times ($\sigma_{on} = 1.06 \pm 0.02$ in PVA compared to 1.85 ± 0.09 on glass). The smaller $-\mu_{off}$ value of 0.37 ± 0.05 in PVA as compared to 1.2 ± 0.1 on glass reveals that back ET is slower in PVA. Additionally, σ_{off} values of 2.03 ± 0.03 and 2.0 ± 0.1 in PVA and on glass, respectively, indicate no change in dispersion between the environments for off-interval times. The changes in μ signify the sensitivity of single-molecule ET dynamics to local conditions, further confirming the environmental dependence of PM605 blinking behavior. The lower σ_{on} and unchanged σ_{off} values for PM605/PVA compared to PM605/glass align with experimental observations that PM605 displays more consistent blinking behavior in

PVA. In fact, this decrease in dispersion may be valuable for BBM, as molecules with more consistent, characteristic blinking are expected to be easier to classify.

3.3.4 Blinking-Based Multiplexing of QD, R6G, and PM605 in PVA

To examine the efficacy of BBM with the addition of PM605, LR is tested on 109 PM605/PVA, 129 QD/PVA, and 112 R6G/PVA emitters. Coefficients for the resulting models are summarized in **Table 3** and corresponding confusion matrices at the default threshold (i.e., $P_A > 0.5$ or 0.33 for binary and ternary comparisons, respectively) are shown in **Figure 11**. Binary comparisons of PM605/PVA against QD/PVA and R6G/PVA yield default classification accuracies of 97.1% and 86.4%, respectively. As expected, this result indicates that the blinking dynamics of R6G and PM605, the two organic fluorophores, are more similar to each other than to QD and are therefore more difficult to distinguish.

LR coefficients in **Table 3** reveal the driving forces for binary classification for the two systems. For the comparison of QD/PVA versus PM605/PVA, $\langle I \rangle_t$ and I_{min} have the largest coefficients (-125.5 and 29.1, respectively) and therefore have the most
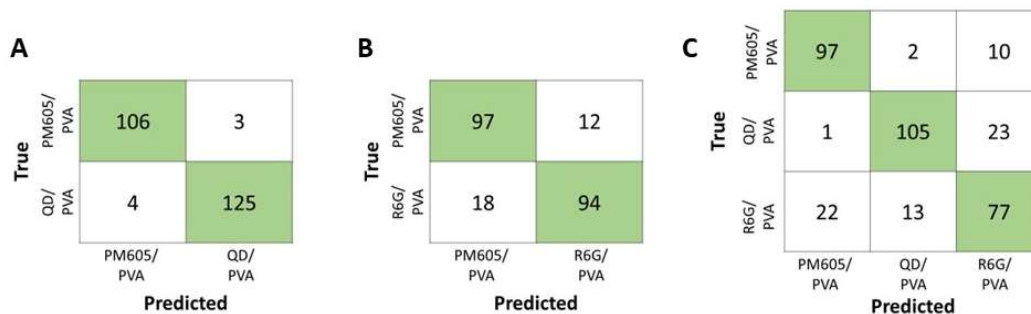
Figure 11. Confusion matrices for BBM of PM605, QD, and R6G in PVA at $P_{exc} = 1$ μW and with the default classification threshold (i.e., $P_A > 0.5$). LR yields classification accuracies of (A) 97.1% for PM605 vs. QD in PVA and (B) 86.4% for PM605 vs. R6G in PVA. (C) Ternary classification of all 3 emitters results in 79.7% accuracy.

influence over classification. The R6G/PVA versus PM605/PVA comparison is driven by the same two blinking statistics with coefficients -8.1 for $\langle I \rangle_t$ and 5.7 for I_{min}. Although $\langle I \rangle_t$ dominates both binary classifications, it does so to a different degree in each comparison. For PM605/PVA versus QD/PVA, the $\langle I \rangle_t$ coefficient of -125.5 is 11.7x greater than the average magnitude of the other nine coefficients (10.7); for PM605/PVA versus R6G/PVA, the corresponding coefficient of -8.1 is just 4.8x above the average (1.7). That is, $\langle I \rangle_t$ is over twice as important for classifying PM605 against QD than R6G in PVA. This result is consistent with the average $\langle I \rangle_t$ values for the emitters, as PM605/PVA and R6G/PVA have more similar averages (7.2 $\pm$ 0.2 and 6.7 $\pm$ 0.4 counts/ 10 ms, respectively) than PM605 and QD (19 $\pm$ 1 counts/ 10 ms), which likely indicates poorer separation of their distributions. Additionally, it is notable that $\langle t_{on,int} \rangle$ and $\langle t_{off,int} \rangle$ play relatively small roles in both binary classifications, despite differences in the lognormal fit parameters for each emitter (**Appendix I, Tables A1-A3**). Therefore, emission intensities, as governed by photostability and ET processes for $\langle I \rangle_t$ and by funamental photophysical parameters for I_{min}, are important factors for classifying PM605 from QD and R6G. However, the temporal durations of on and off intervals, which also rely on ET dynamics, exert only modest influence over LR predictions.

To examine the achievable level of accuracy, classification thresholding is applied to the LR comparison of R6G/PVA and PM605/PVA. As previously described, elevating this threshold increases accuracy and TPR and decreases FPR by discarding less certain emitters. When the threshold is shifted from 0.5 to 0.84, classification

accuracy rises from 86.4% to 95% with 73.8% data retention. Because LR already classifies PM605 and QD in PVA with incredibly high default accuracy (97.1%), no thresholding is required.

When a ternary LR classification is performed using all three emitters, the default accuracy decreases to 79.7%. For ternary comparisons, the default threshold is 0.33 instead of 0.5, so the standard for classification is lower. Once again, a 95% accuracy is achieved by increasing the classification threshold to 0.95 but results in 64.6% data loss. However, for applications that are sensitive to data retention, accuracies as high as 89.8% can be reached with data loss of only 30%. Using classification thresholding, BBM results are highly tunable depending on the desired balance of accuracy and data retention. Overall, despite the observation of dispersive blinking behavior in QD, R6G, and PM605 in the heterogenous PVA environment, LR predicts emitter identity with incredible success.

3.4 Conclusion

These studies expand the capabilities of BBM by investigating its performance in multiplexing emitters in complex polymer matrix and by introducing an additional fluorophore, PM605, to the already-established QD/R6G system. SMS is used to collect blinking dynamics of each of the emitters, which are then quantified and classified by CPD and LR, respectively. Testing BBM in PVA establishes the viability of the method for biological imaging applications because it models the complexity and heterogeneity of a biological system. Despite additional challenges with the

polymer environment, emitters are discriminated from PVA background signal by applying a simple intensity threshold for diffraction-limited spots. When embedded in PVA matrix, QD and R6G emitters undergo different ET processes than observed previously on glass. LR adapts to these changes to rapidly generate new models with coefficients that reflect alterations in the distributions of CPD statistics, yielding default accuracy of 86.7% and reaching as high as 95% when the classification threshold is increased.

Blinking dynamics of PM605 on glass and in PVA are studied in order to examine its blinking mechanism in each environment and, ultimately, add this third small-molecule emitter to the library of spectrally-overlapped probes for BBM. The lognormally distributed on- and off-interval times for PM605 on glass and in PVA are consistent with the Albery model for complex ET. Although blinking is attributed to ET in both environments, fit parameters $-\mu$ and σ reveal faster ET, slower BET, and lower dispersion for PM605 in PVA than on glass. Harnessing PM605 blinking for BBM, LR classification of PM605/PVA against QD/PVA and R6G/PVA reveals binary default accuracies of 86.4% and 97.1%, respectively. Ternary classification of all three emitters in PVA yields lower accuracy (79.7%) at the default threshold. However, in all three cases, accuracy is highly tunable by adjusting the classification threshold depending on the needs of the experiment and the availability of data.

The experiments in this thesis demonstrate the incredible potential of BBM for high accuracy classification of any system of spectrally-overlapped emitters under numerous experimental conditions, even conditions that add significantly to the

complexity of the system of study. The next steps are to continue to expand the palette of BBM probes and to further optimize BBM accuracy and efficiency. Current research in the Wustholz lab is exploring the performance of BBM with multiple rhodamine dyes. The effects of emitter concentration are also being tested, as SRI experiments require labeling densities that are higher than what is typical for single-molecule studies.[44] Additionally, in the near future, blinking data will be collected using wide-field acquisition on an electron multiplying charge coupled device camera, which will accelerate data collection and increase the size of datasets.

Overall, BBM is a powerful new alternative to current multicolor SRI techniques, which are limited in scope and efficiency due to their reliance on spectral color for emitter identification. Demonstrating rapid, automated, and accurate classification of three emitters in a PVA environment using LR reveals the viability of BBM for imaging complex biological systems.

References

(1)   Cohen, S.; Valm, A. M.; Lippincott-Schwartz, J. Interacting Organelles. *Curr. Opin. Cell Biol.* **2018**, *53*, 84–91. https://doi.org/10.1016/j.ceb.2018.06.003.

(2)   Valm, A. M.; Cohen, S.; Legant, W. R.; Melunis, J.; Hershberg, U.; Wait, E.; Cohen, A. R.; Davidson, M. W.; Betzig, E.; Lippincott-Schwartz, J. Applying Systems-Level Spectral Imaging and Analysis to Reveal the Organelle Interactome. *Nature* **2017**, *546* (7656), 162–167. https://doi.org/10.1038/nature22369.

(3)   Huang, B.; Babcock, H.; Zhuang, X. Breaking the Diffraction Barrier: Super-Resolution Imaging of Cells. *Cell* **2010**, *143* (7), 1047–1058. https://doi.org/10.1016/j.cell.2010.12.002.

(4)   Birk, U. J. *Super-Resolution Microscopy: A Practical Guide*; John Wiley & Sons, Incorporated: Newark, GERMANY, 2017.

(5)   Lelek, M.; Gyparaki, M. T.; Beliu, G.; Schueder, F.; Griffié, J.; Manley, S.; Jungmann, R.; Sauer, M.; Lakadamyali, M.; Zimmer, C. Single-Molecule Localization Microscopy. *Nat. Rev. Methods Primer* **2021**, *1* (1), 1–27. https://doi.org/10.1038/s43586-021-00038-x.

(6)   Tam, J.; Cordier, G. A.; Borbely, J. S.; Álvarez, Á. S.; Lakadamyali, M. Cross-Talk-Free Multi-Color STORM Imaging Using a Single Fluorophore. *PLOS ONE* **2014**, *9* (7), e101772. https://doi.org/10.1371/journal.pone.0101772.

(7)   Valley, C. C.; Liu, S.; Lidke, D. S.; Lidke, K. A. Sequential Superresolution Imaging of Multiple Targets Using a Single Fluorophore. *PLOS ONE* **2015**, *10* (4), e0123941. https://doi.org/10.1371/journal.pone.0123941.

(8)   DeSalvo, G. A.; Hoy, G. R.; Kogan, I. M.; Li, J. Z.; Palmer, E. T.; Luz-Ricca, E.; de Gialluly, P. S.; Wustholz, K. L. Blinking-Based Multiplexing: A New Approach for Differentiating Spectrally Overlapped Emitters. *J. Phys. Chem. Lett.* **2022**, *13* (22), 5056–5060. https://doi.org/10.1021/acs.jpclett.2c01252.

(9)   Moerner, W. E. (William E.). Nobel Lecture: Single-Molecule Spectroscopy, Imaging, and Photocontrol: Foundations for Super-Resolution Microscopy. *Rev. Mod. Phys.* **2015**, *87* (4), 1183–1212. https://doi.org/10.1103/RevModPhys.87.1183.

(10)   Hoy, G. R.; DeSalvo, G. A.; Haile, S. H.; Smith, E. N.; Wustholz, K. L. Rapid, Accurate Classification of Single Emitters in Various Conditions and Environments for Blinking-Based Multiplexing. *J. Phys. Chem. A* **2023**, *127* (15), 3518–3525. https://doi.org/10.1021/acs.jpca.3c00917.

(11)   Nthoiwa, K. K. M.; Diaz, C. A.; Chaudhari, Y. Vinyl Alcohol Polymers.

(12)   Hallensleben, M. L.; Fuss, R.; Mummy, F. Polyvinyl Compounds, Others. In *Ullmann's Encyclopedia of Industrial Chemistry*; Wiley-VCH Verlag GmbH & Co. KGaA, Ed.; Wiley-VCH Verlag GmbH & Co. KGaA: Weinheim, Germany, 2015; pp 1–23. https://doi.org/10.1002/14356007.a21_743.pub2.

(13)   Sluss, D.; Bingham, C.; Burr, M.; D. Bott, E.; A. Riley, E.; J. Reid, P. Temperature-Dependent Fluorescence Intermittency for Single Molecules of

Violamine R in Poly(Vinyl Alcohol). *J. Mater. Chem.* **2009**, *19* (40), 7561–7566. https://doi.org/10.1039/B909076B.

(14) Zondervan, R.; Kulzer, F.; Kol'chenk, M. A.; Orrit, M. Photobleaching of Rhodamine 6G in Poly(Vinyl Alcohol) at the Ensemble and Single-Molecule Levels. *J. Phys. Chem. A* **2004**, *108* (10), 1657–1665. https://doi.org/10.1021/jp037222e.

(15) Dibbern-Brunelli, D.; de Oliveira, M. G.; Atvars, T. D. Z. Temperature Dependence of the Photobleaching Process of Fluorescein in Poly(Vinyl Alcohol). *J. Photochem. Photobiol. Chem.* **1995**, *85* (3), 285–289. https://doi.org/10.1016/1010-6030(94)03915-H.

(16) Talhavini, M.; Atvars, T. D. Z. Photostability of Xanthene Molecules Trapped in Poly(Vinyl Alcohol) (PVA) Matrices. *J. Photochem. Photobiol. Chem.* **1999**, *120* (2), 141–149. https://doi.org/10.1016/S1010-6030(98)00416-X.

(17) Talhavini, M.; Atvars, T. D. Z. Dye-Polymer Interactions Controlling the Kinetics of Fluorescein Photobleaching Reactions in Poly(Vinyl Alcohol). *J. Photochem. Photobiol. Chem.* **1998**, *114* (1), 65–73. https://doi.org/10.1016/S1010-6030(97)00307-9.

(18) Testa, I.; Wurm, C. A.; Medda, R.; Rothermel, E.; Von Middendorf, C.; Fölling, J.; Jakobs, S.; Schönle, A.; Hell, S. W.; Eggeling, C. Multicolor Fluorescence Nanoscopy in Fixed and Living Cells by Exciting Conventional Fluorophores with a Single Wavelength. *Biophys. J.* **2010**, *99* (8), 2686–2694. https://doi.org/10.1016/j.bpj.2010.08.012.

(19) Zondervan, R.; Kulzer, F.; Orlinskii, S. B.; Orrit, M. Photoblinking of Rhodamine 6G in Poly(Vinyl Alcohol): Radical Dark State Formed through the Triplet. *J. Phys. Chem. A* **2003**, *107* (35), 6770–6776. https://doi.org/10.1021/jp034723r.

(20) Issac, A.; von Borczyskowski, C.; Cichos, F. Correlation between Photoluminescence Intermittency of CdSe Quantum Dots and Self-Trapped States in Dielectric Media. *Phys. Rev. B* **2005**, *71* (16), 161302. https://doi.org/10.1103/PhysRevB.71.161302.

(21) Bittel, A. M.; Nickerson, A.; Saldivar, I. S.; Dolman, N. J.; Nan, X.; Gibbs, S. L. Methodology for Quantitative Characterization of Fluorophore Photoswitching to Predict Superresolution Microscopy Image Quality. *Sci. Rep.* **2016**, *6*, 29687. https://doi.org/10.1038/srep29687.

(22) Bittel, A. M.; Saldivar, I. S.; Dolman, N. J.; Nan, X.; Gibbs, S. L. Superresolution Microscopy with Novel BODIPY-Based Fluorophores. *PLOS ONE* **2018**, *13* (10), e0206104. https://doi.org/10.1371/journal.pone.0206104.

(23) Ishitobi, H.; Kai, T.; Fujita, K.; Sekkat, Z.; Kawata, S. On Fluorescence Blinking of Single Molecules in Polymers. *Chem. Phys. Lett.* **2009**, *468* (4), 234–238. https://doi.org/10.1016/j.cplett.2008.12.025.

(24) Rivera-Hernández, G.; Antunes-Ricardo, M.; Martínez-Morales, P.; Sánchez, M. L. Polyvinyl Alcohol Based-Drug Delivery Systems for Cancer Treatment. *Int. J. Pharm.* **2021**, *600*, 120478. https://doi.org/10.1016/j.ijpharm.2021.120478.

(25) Engelke, L.; Winter, G.; Engert, J. Application of Water-Soluble Polyvinyl Alcohol-Based Film Patches on Laser Microporated Skin Facilitates Intradermal Macromolecule and Nanoparticle Delivery. *Eur. J. Pharm. Biopharm.* **2018**, *128*, 119–130. https://doi.org/10.1016/j.ejpb.2018.04.008.

(26) Marin, Ştefania; Albu Kaya, M. G.; Ghica, M. V.; Dinu-Pîrvu, C.; Popa, L.; Udeanu, D. I.; Mihai, G.; Enachescu, M. Collagen-Polyvinyl Alcohol-Indomethacin Biohybrid Matrices as Wound Dressings. *Pharmaceutics* **2018**, *10* (4), 224. https://doi.org/10.3390/pharmaceutics10040224.

(27) Chen, J.; Zheng, M.; Tan, K. B.; Lin, J.; Chen, M.; Zhu, Y. Polyvinyl Alcohol/Xanthan Gum Composite Film with Excellent Food Packaging, Storage and Biodegradation Capability as Potential Environmentally-Friendly Alternative to Commercial Plastic Bag. *Int. J. Biol. Macromol.* **2022**, *212*, 402–411. https://doi.org/10.1016/j.ijbiomac.2022.05.119.

(28) Wijesooriya, C. S.; Peterson, J. A.; Shrestha, P.; Gehrmann, E. J.; Winter, A. H.; Smith, E. A. A Photoactivatable BODIPY Probe for Localization-Based Super-Resolution Cellular Imaging. *Angew. Chem.* **2018**, *130* (39), 12867–12871. https://doi.org/10.1002/ange.201805827.

(29) Adhikari, S.; Moscatelli, J.; Puchner, E. Live Cell Super-Resolution Imaging with Red-Shifted States of Conventional Bodipy Fluorophores. *Biophys. J.* **2019**, *116* (3, Supplement 1), 439a–440a. https://doi.org/10.1016/j.bpj.2018.11.2366.

(30) Adhikari, S.; Moscatelli, J.; Smith, E. M.; Banerjee, C.; Puchner, E. M. Single-Molecule Localization Microscopy and Tracking with Red-Shifted States of Conventional BODIPY Conjugates in Living Cells. *Nat. Commun.* **2019**, *10* (1), 3400. https://doi.org/10.1038/s41467-019-11384-6.

(31) Bittel, A. M.; Davis, A. M.; Wang, L.; Nederlof, M. A.; Escobedo, J. O.; Strongin, R. M.; Gibbs, S. L. Varied Length Stokes Shift BODIPY-Based Fluorophores for Multicolor Microscopy. *Sci. Rep.* **2018**, *8* (1), 4590. https://doi.org/10.1038/s41598-018-22892-8.

(32) Kowada, T.; Maeda, H.; Kikuchi, K. BODIPY-Based Probes for the Fluorescence Imaging of Biomolecules in Living Cells. *Chem. Soc. Rev.* **2015**, *44* (14), 4953–4972. https://doi.org/10.1039/C5CS00030K.

(33) Zhai, D.; Lee, S.-C.; Vendrell, M.; Leong, L. P.; Chang, Y.-T. Synthesis of a Novel BODIPY Library and Its Application in the Discovery of a Fructose Sensor. *ACS Comb. Sci.* **2012**, *14* (2), 81–84. https://doi.org/10.1021/co200136b.

(34) Loudet, A.; Burgess, K. BODIPY Dyes and Their Derivatives: Syntheses and Spectroscopic Properties. *Chem. Rev.* **2007**, *107* (11), 4891–4932. https://doi.org/10.1021/cr078381n.

(35) Ulrich, G.; Ziessel, R.; Harriman, A. The Chemistry of Fluorescent Bodipy Dyes: Versatility Unsurpassed. *Angew. Chem. Int. Ed.* **2008**, *47* (7), 1184–1201. https://doi.org/10.1002/anie.200702070.

(36) Riley, E. A.; Bingham, C.; Bott, E. D.; Kahr, B.; Reid, P. J. Two Mechanisms for Fluorescence Intermittency of Single Violamine R Molecules. *Phys. Chem. Chem. Phys.* **2011**, *13* (5), 1879–1887. https://doi.org/10.1039/C0CP01716G.

(37) Wong, N. Z.; Ogata, A. F.; Wustholz, K. L. Dispersive Electron-Transfer Kinetics from Single Molecules on TiO2 Nanoparticle Films. *J. Phys. Chem. C* **2013**, *117* (41), 21075–21085. https://doi.org/10.1021/jp405899v.

(38) Zondervan, R.; Kulzer, F.; Mathies, G.; Orrit, M. Non-Exponential Kinetics of Photoblinking and Photobleaching of Rhodamine 6G in Polyvinylalcohol. *Single Mol.* **2002**, *3* (5–6), 317–318. https://doi.org/10.1002/1438-5171(200211)3:5/6<317::AID-SIMO317>3.0.CO;2-C.

(39) Gensch, T.; Böhmer, M.; Aramendía, P. F. Single Molecule Blinking and Photobleaching Separated by Wide-Field Fluorescence Microscopy. *J. Phys. Chem. A* **2005**, *109* (30), 6652–6658. https://doi.org/10.1021/jp0510847.

(40) Liu, J.; Hill, C. M.; Pan, S.; Liu, H. Interfacial Charge Transfer Events of BODIPY Molecules: Single Molecule Spectroelectrochemistry and Substrate Effects. *Phys. Chem. Chem. Phys.* **2014**, *16* (42), 23150–23156. https://doi.org/10.1039/C4CP02950J.

(41) Albery, W. J.; Bartlett, P. N.; Wilde, C. P.; Darwent, J. R. A General Model for Dispersed Kinetics in Heterogeneous Systems. *J. Am. Chem. Soc.* **1985**, *107* (7), 1854–1858. https://doi.org/10.1021/ja00293a008.

(42) Kopera, K. M.; Tuckman, H. G.; Hoy, G. R.; Wustholz, K. L. Origin of Kinetic Dispersion in Eosin-Sensitized TiO2: Insights from Single-Molecule Spectroscopy. *J. Phys. Chem. C* **2021**, *125* (43), 23634–23645. https://doi.org/10.1021/acs.jpcc.1c07597.

(43) Tan, J. A.; Rose, J. T.; Cassidy, J. P.; Rohatgi, S. K.; Wustholz, K. L. Dispersive Electron-Transfer Kinetics of Rhodamines on TiO2: Impact of Structure and Driving Force on Single-Molecule Photophysics. *J. Phys. Chem. C* **2016**, *120* (37), 20710–20720. https://doi.org/10.1021/acs.jpcc.6b01960.

(44) Burgert, A.; Letschert, S.; Doose, S.; Sauer, M. Artifacts in Single-Molecule Localization Microscopy. *Histochem. Cell Biol.* **2015**, *144* (2), 123–131. https://doi.org/10.1007/s00418-015-1340-4.

Appendix I. On and Off Time Distributions and Fit Parameters
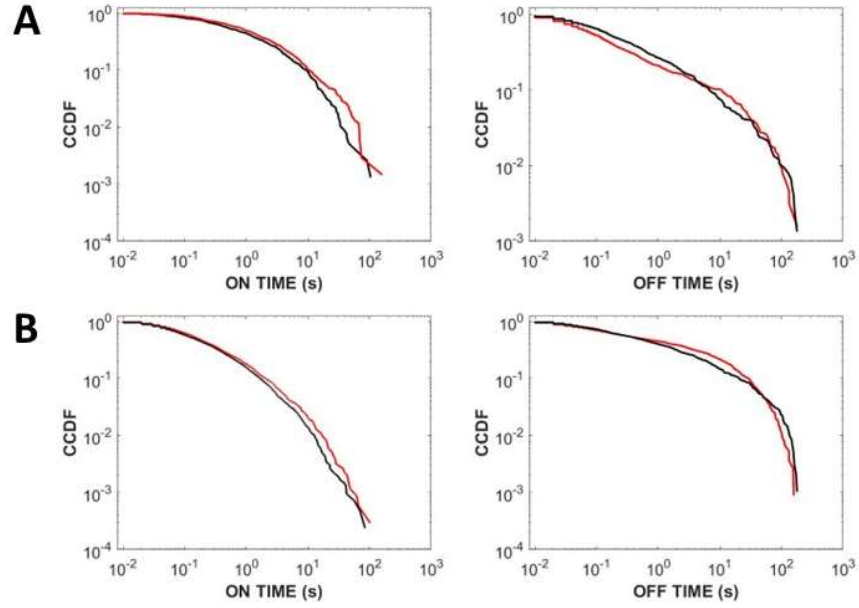
Figure 1. CCDF plots of (A) on and off intervals and (B) on and off segments for R6G/glass (black) and R6G/PVA (red).

	Power Law: $\frac{\alpha-1}{t_{min}}(\frac{t}{t_{min}})^{-\alpha}$			Weibull: $\frac{A}{B}\left(\frac{t}{B}\right)^{A-1}e^{-\left(\frac{t}{B}\right)^{A}}$			Lognormal: $\frac{1}{t\sigma\sqrt{2\pi}}e^{-\frac{(\ln(t)-\mu)^2}{2\sigma^2}}$		
	$t_{min}(s)$	α	p	A	B	p	μ	σ	p
ON INT	5.57	2.09 ± 0.04	0.056	0.551 ± 0.007	2.4 ± 0.1	0	-0.05 ± 0.07	1.91 ± 0.05	0.078
OFF INT	0.06	1.43 ± 0.02	0.017	0.391 ± 0.006	0.74 ± 0.05	0	-1.60 ± 0.09	2.31 ± 0.06	0
ON SEG	0.79	1.89 ± 0.01	0	0.570 ± 0.003	0.51 ± 0.01	0	-1.59 ± 0.03	1.67 ± 0.02	0
OFF SEG	28.84	2.66 ± 0.05	0.001	0.401 ± 0.005	2.7 ± 0.1	0	-0.36 ± 0.08	2.66 ± 0.06	0

Table 1. Power law, Weibull, and lognormal distribution best fit parameters (with standard deviations) and p-values of 683 on-interval, 643 off-interval, 3,420 on-segment, and 1,127 off segment times for 112 R6G/PVA emitters at $P_{exc} = 1$ μW.
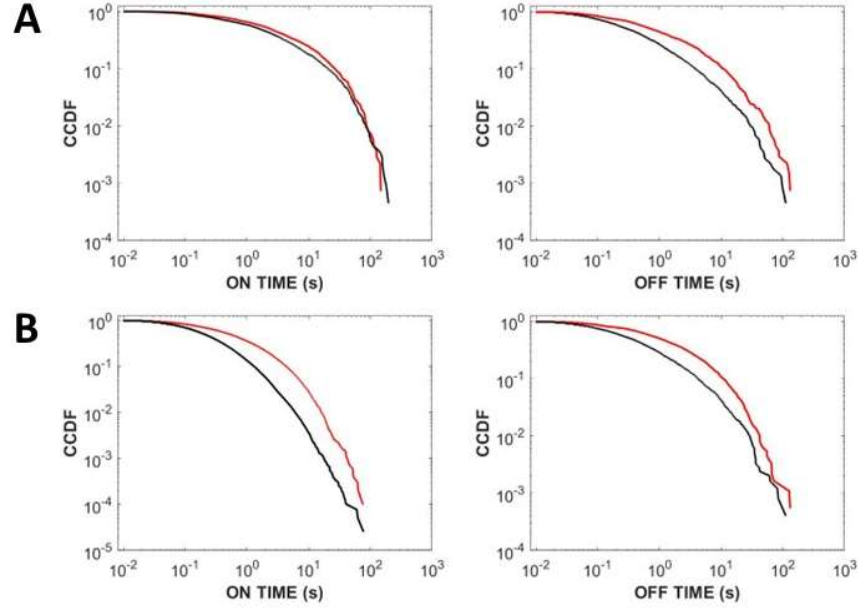
Figure 2. CCDF plots of (A) on and off intervals and (B) on and off segments for QD/glass (black) and QD/PVA (red).

	Power Law: $\frac{\alpha-1}{t_{min}}(\frac{t}{t_{min}})^{-\alpha}$			Weibull: $\frac{A}{B}\left(\frac{t}{B}\right)^{A-1}e^{-\left(\frac{t}{B}\right)^{A}}$			Lognormal: $\frac{1}{t\sigma\sqrt{2\pi}}e^{-\frac{(\ln(t)-\mu)^2}{2\sigma^2}}$		
	$t_{min}(s)$	α	p	A	B	p	μ	σ	p
ON INT	13.99	2.29 ± 0.04	0	0.571 ± 0.004	5.6 ± 0.2	0	0.78 ± 0.05	1.90 ± 0.04	0.001
OFF INT	13.29	2.49 ± 0.04	0.085	0.521 ± 0.005	2.05 ± 0.08	0	-0.26 ± 0.05	1.97 ± 0.04	0
ON SEG	14.57	3.70 ± 0.03	0.222	0.650 ± 0.002	1.14 ± 0.01	0	-0.70 ± 0.02	1.66 ± 0.01	0
OFF SEG	20.78	3.32 ± 0.05	0.709	0.580 ± 0.004	2.39 ± 0.08	0	-0.06 ± 0.04	1.89 ± 0.03	0

Table 2. Power law, Weibull, and lognormal distribution best fit parameters (with standard deviations) and p-values of 1,358 on-interval, 1,345 off-interval, 10,110 on-segment, and 1,832 off-segment times for 129 QD/PVA emitters at $P_{exc} = 1$ µW.
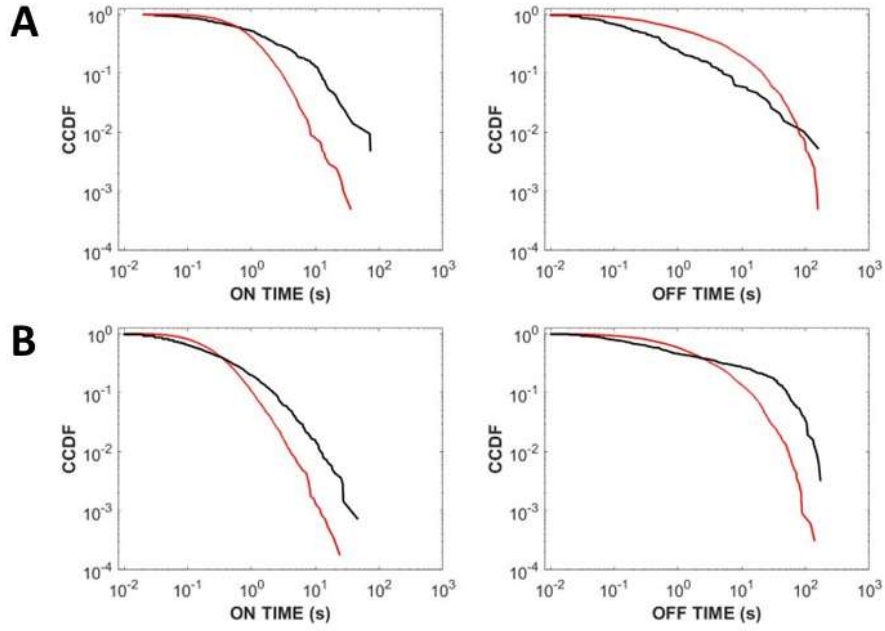
Figure 3. CCDF plots of (A) on and off intervals and (B) on and off segments for PM605/glass (black) and PM605/PVA (red).

	Power Law: $\frac{\alpha-1}{t_{min}}(\frac{t}{t_{min}})^{-\alpha}$			Weibull: $\frac{A}{B}\left(\frac{t}{B}\right)^{A-1} e^{-\left(\frac{t}{B}\right)^{A}}$			Lognormal: $\frac{1}{t\sigma\sqrt{2\pi}}e^{-\frac{(\ln(t)-\mu)^2}{2\sigma^2}}$		
	$t_{min}(s)$	α	p	A	B	p	μ	σ	p
ON INT	2.84	3.04 ± 0.05	0.68	0.940 ± 0.005	1.30 ± 0.06	0	-0.26 ± 0.02	1.06 ± 0.02	0.041
OFF INT	41.57	3.34 ± 0.05	0.112	0.531 ± 0.004	3.9 ± 0.1	0	0.37 ± 0.05	2.03 ± 0.03	0
ON SEG	0.81	2.57 ± 0.02	0.004	0.880 ± 0.003	0.46 ± 0.01	0	-1.36 ± 0.01	1.11 ± 0.01	0
OFF SEG	17.36	2.90 ± 0.03	0.041	0.600 ± 0.003	3.17 ± 0.07	0	0.30 ± 0.03	1.77 ± 0.02	0.003

Table 3. Power law, Weibull, and lognormal distribution best fit parameters (with standard deviations) and p-values of 2,032 on-interval, 2,032 off-interval, 5,646 on-segment, and 3,293 off-segment times for 109 PM605/PVA emitters at P_{exc} = 1 µW.

	Power Law: $\frac{\alpha-1}{t_{min}}(\frac{t}{t_{min}})^{-\alpha}$			Weibull: $\frac{A}{B}\left(\frac{t}{B}\right)^{A-1}e^{-\left(\frac{t}{B}\right)^A}$			Lognormal: $\frac{1}{t\sigma\sqrt{2\pi}}e^{-\frac{(\ln(t)-\mu)^2}{2\sigma^2}}$		
	$t_{min}(s)$	α	p	A	B	p	μ	σ	p
ON INT	10.52	2.9 ± 0.1	0.967	0.58 ± 0.01	2.5 ± 0.3	0.009	0.0 ± 0.1	1.85 ± 0.09	0.586
OFF INT	0.42	1.63 ± 0.05	0.055	0.46 ± 0.01	0.9 ± 0.1	0	-1.2 ± 0.1	2.0 ± 0.1	0.032
ON SEG	1.91	2.28 ± 0.03	0.021	0.610 ± 0.006	0.54 ± 0.02	0	-1.51 ± 0.04	1.67 ± 0.03	0
OFF INT	43.08	2.9 ± 0.1	0.041	0.378 ± 0.009	4.1 ± 0.4	0	0.1 ± 0.1	2.6 ± 0.1	0

Table 4. Power law, Weibull, and lognormal distribution best fit parameters (with standard deviations) and p-values of 211 on-interval, 192 off-interval, 1,392 on-segment, and 313 off-segment times for 118 PM605/glass emitters at P_{exc} = 0.8 µW.

Blinking Statistic	PM605/glass	PM605/PVA
N_I	4.8 ± 0.3	8.1 ± 0.2
$N_{on,seg}$	12 ± 3	52 ± 4
$N_{off,seg}$	2.7 ± 0.4	30 ± 1
$N_{on,int}$	1.8 ± 0.4	19 ± 1
$N_{off,int}$	1.6 ± 0.4	19 ± 1
I_{min}	9.5 ± 0.2	8.4 ± 0.2
I_{max}	37 ± 4	31 ± 1
$\langle I \rangle_t$	9.0 ± 0.6	7.2 ± 0.2
$\langle t_{on,seg} \rangle$	2.7 ± 0.4	0.60 ± 0.03
$\langle t_{off,seg} \rangle$	28 ± 3	6.8 ± 0.4
$\langle t_{on,int} \rangle$	8 ± 1	1.6 ± 0.1
$\langle t_{off,int} \rangle$	6 ± 2	11 ± 1

Table A5. Average blinking statistics of PM605 molecules at P_{exc} = 0.8 µW on glass and P_{exc} = 1 µW in PVA, respectively. Errors correspond to standard deviations of the mean. Intensities are reported in counts/ 10 ms, and values for $\langle t \rangle$ are reported in seconds.